Department of Physics and Astronomy
University of Heidelberg

Bachelor Thesis in Physics
submitted by

Florian Frauen

born in Elmshorn (Germany)

2021

Characterisation of the time resolution of the MuPix10 pixel sensor

This Bachelor Thesis has been carried out by Florian Frauen at the
Physikalisches Institut in Heidelberg
under the supervision of
Prof. André Schöning

Abstract

The Mu3e experiment searches for the charged lepton flavor violating decay $\mu^+ \to e^+e^-e^+$ with a planned sensitivity of 1×10^{-16}. This requires a pixel detector with high momentum and time resolution. The MuPix10 is the first full-scale prototype designed for this purpose. The object of this thesis is the characterisation of the MuPix10 in terms of time resolution, with the final goal of identifying the limiting features of the design and providing input to the design of the MuPix11, which will be the sensor used in the Mu3e experiment. The result of this characterisation shows that the MuPix10 achieves a time resolution of (14.8 ± 0.9) ns before and (8.06 ± 0.07) ns after corrections. The limiting factors of the time resolution have been identified as the pixel-to-pixel delay of (5.53 ± 0.06) ns and the single pixel time resolution of (6.0 ± 1.0) ns. Furthermore, a new feature of the MuPix10, the ToT-cap, and its influence on the time resolution are investigated.

Kurzfassung

Das Mu3e Experiment sucht mit einer geplanten Sensitivität von 1×10^{-16} nach dem geladenen Lepton-flavour verletzenden Zerfall $\mu^+ \to e^+e^-e^+$. Dafür wird ein Pixeldetektor mit einer hohen Impuls- und Zeitauflösung benötigt. Der MuPix10 ist der erste solche Prototyp mit der richtigen Dimensionierung. In dieser Arbeit wird der MuPix10 mit Hinblick auf die Zeitauflösung charakterisiert, um schließlich die Eigenschaften des Designs zu finden, die die Zeitauflösung beschränken und Anregungen für das Design des MuPix11, des Sensors der im Mu3e Experiment verwendet werden soll, zu geben. Das Ergebnis der Charakterisierung ist, dass der MuPix10 eine Zeitauflösung von (14.8 ± 0.9) ns vor und (8.06 ± 0.07) ns nach Korrekturen erreicht. Die beschränkenden Faktoren sind die Pixel-zu-Pixel-Latenz in Höhe mit (5.53 ± 0.06) ns und die Zeitauflösung eines einzelnen Pixels von (6.0 ± 1.0) ns. Weiterhin wurden eine neue Eigenschaft des MuPix10, die ToT-cap, und ihr Einfluss auf die Zeitauflösung untersucht.

Contents

Part I

Theory

1 Introduction

The Standard Model of Particle Physics describes all known particles and three of the four fundamental interactions between them. It is a well tested theory. However, there are some phenomena like dark matter or the asymmetry of matter and anti-matter which can not be explained by it. We therefore know that the Standard Model is incomplete.

There are two basic approaches when searching for new particles: One can either try to go to higher energies to directly produce and observe them. The other way is to go to high intensities to find small deviations from the branching ratios predicted by the Standard Model which are caused by decay channels mediated through these new particles.

The Mu3e experiment follows the second approach. It will search for the charged lepton flavour violating decay $\mu^+ \to e^+e^-e^+$. While this decay is in theory possible, the predicted branching ratio in the Standard Model of 2.1×10^{-55} is too small to be observed in any experiment in the near future [1]. However, some theories beyond the Standard Model predict much higher branching ratios. The Mu3e experiment plans to observe $\mu^+ \to e^+e^-e^+$ decays with a sensitivity of 2×10^{-15} in its final phase [2]. This is four orders of magnitudes higher than the current limit of 1×10^{-12} which was established by the SINDRUM experiment in 1988 [3]. To distinguish real $\mu^+ \to e^+e^-e^+$ decays from background events, a high momentum and time resolution is needed [4]. To achieve this goal the Mu3e experiment develops its own pixel sensor series, called the MuPix sensors. The MuPix10 is the first full-scale prototype for the Mu3e experiment. Based on the experiences with the MuPix10, the MuPix11 will be designed to be the final MuPix sensor which fulfills all the requirements for the Mu3e experiment.

In this thesis the time resolution of the MuPix10 is studied. The configuration of the MuPix10 is optimised with respect to the time resolution in the first part. In the second part, the optimised sensor is characterised: different features are investigated to find the limiting factors for the time resolution. The insights from this characterisation can be utilised in the design of the MuPix11.

2 The Standard Model of Particle Physics

The Standard Model of Particle Physics (SM) is a quantum field theory describing the elementary particles and three of the four known fundamental interactions between them. Each particle can be identified by its mass and certain quantum numbers, namely the spin and the charges of each force: colour for the strong interaction, electric charge for the electromagnetic interaction and weak isospin for the weak interaction.

The half integer spin particles are called fermions. They form all known matter. There are twelve different fermions and for each of them an antiparticle, which has inverted charges, but is otherwise the same.

Interactions between them are mediated by gauge bosons with integer spin. The gluons carry the strong interaction, the W^+, W^- and the Z^0 boson the weak interaction and the photon the electromagnetic interaction.

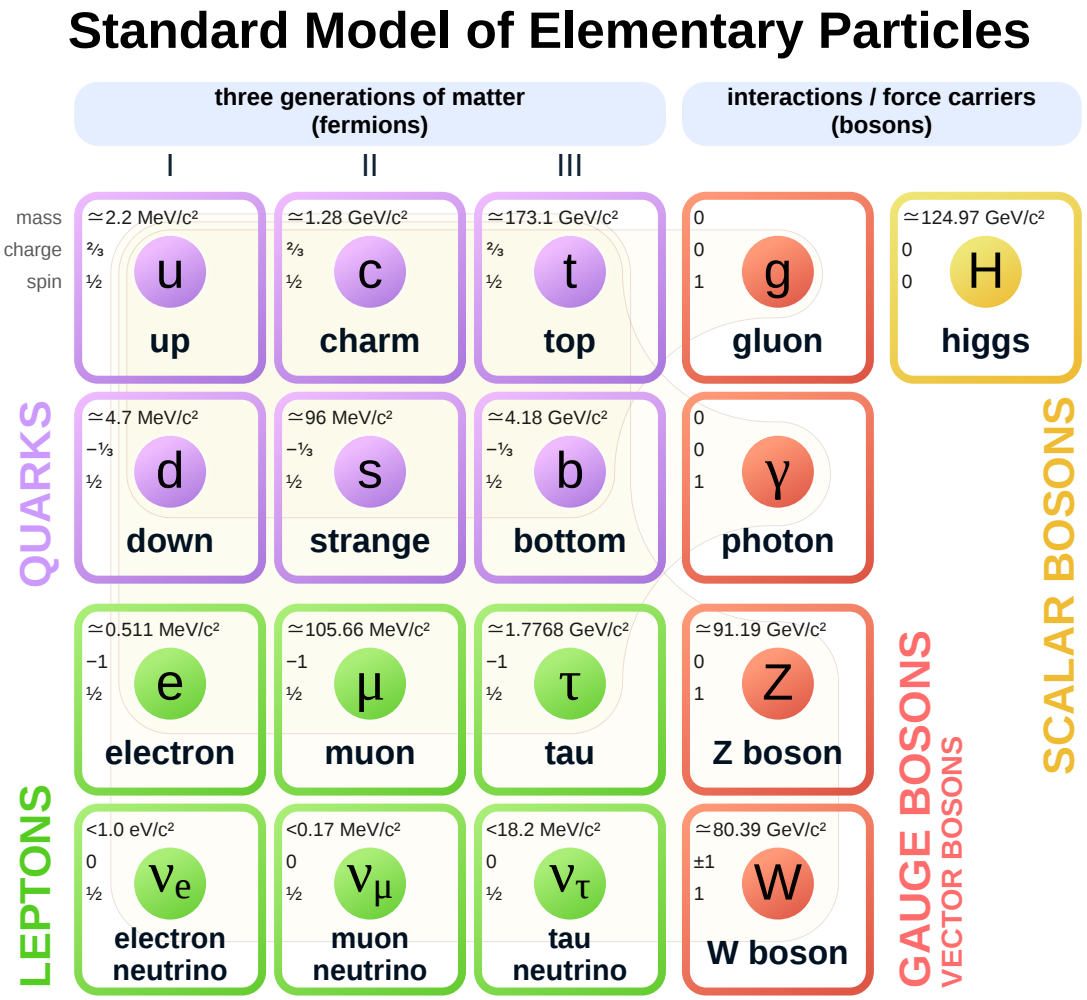

Figure 1: The Standard Model of Elementary Particles [5]

The fermions can be divided in two groups, the first of which is the quarks. There are three quarks with charge $+2/3$ and three quarks with charge $-1/3$. They are ordered in generations according to their mass (Fig. 1). The quarks participate in all three interactions and they are the only fermions with colour. That means that they can not be found freely but only in confined states of neutral colour.
The other group is the leptons, which can also be ordered into generations. Each generation consists of a charged particle and a neutrino, which is neutral. Neutrinos can only interact via the weak force while the charged particles can also interact via the electromagnetic force.
The count of particles from each lepton generation minus the respective antiparticles is the lepton flavour. Lepton flavour is not conserved as lepton flavour violation was observed in neutrino oscillations [6, 7, 8]. However, between charged leptons no lepton flavour violation was seen so far.
In principle the SM allows these charged lepton flavour violations (cLFV) via neutrino oscillations (Fig. 2). However, the branching ratio (BR) of 2.1×10^{-55} is so low that cLFV would not be observable in any experiment in the near future [1].
So far the SM has been tested quite well, but there are some phenomena as for example dark matter and the asymmetry between matter and anti-matter which can not be described by it. This has caused the development of new theories beyond the Standard Model (BSM theories). Some of them predict cLFVs at much higher rates. For example the Supersymmetry framework (SUSY) allows the cLFV decay $\mu^+ \to e^+e^-e^+$ via heavy mediators (Fig. 3). The observation of cLFV would be a clear sign of BSM physics and its rate would indicate which BSM theories might be right.

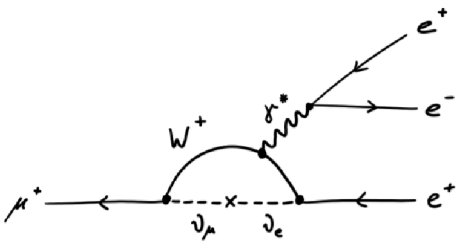

Figure 2: $\mu^+ \to e^+e^-e^+$ decay via neutrino oscillation [9]

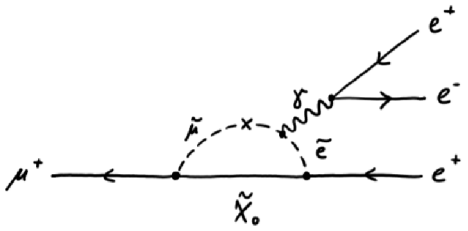

Figure 3: $\mu^+ \to e^+e^-e^+$ decay in the SUSY framework via a heavy mediator [9]

3 The Mu3e experiment

Many experiments have searched for cLFV. The current upper limit for the BR of the $\mu^+ \to e^+e^-e^+$ decay of 1×10^{-12} was established by the SINDRUM experiment in 1988 [3]. The Mu3e experiment plans to detect $\mu^+ \to e^+e^-e^+$ decays with a sensitivity of 2×10^{-15} in its first phase and 1×10^{-16} in its second phase at the 90% confidence level [2]. For this two things are necessary: First, a high intensity muon beam to accumalate enough statistics in a reasonable time. Second, a high momentum and time resolution to distinguish real $\mu^+ \to e^+e^-e^+$ decays from background events.
The muon beam line $\pi E5$ at PSI has a beam rate of $\approx 1 \times 10^8$ Hz which is enough for the first phase. The second phase can start after the planned new High Intensity Muon Beamline (HIMB) with a intensity of $\approx 2 \times 10^9$ Hz is finished [4].

3.1 Signal decay

The signal decay $\mu^+ \to e^+e^-e^+$ has two properties that can be used to distinguish it from the background. First, from momentum and energy conservation (Eq. 1 and 2) in the rest system of the muon follows, that each electron or positron can have a maximum energy of $E < \frac{m_\mu c^2}{2} = 53\,\text{MeV}$.
Second, since the muons are stopped by the target before they decay, the decay must be point-like.

$$\vec{p}_{tot} = \sum_i \vec{p}_i = 0 \tag{1}$$

$$E_{tot} = \sum_i E_i = m_\mu c^2 \tag{2}$$

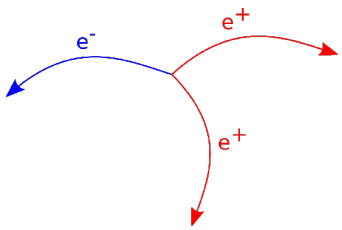

Figure 4: Signal decay

3.2 Background

3.2.1 Irreducible background

The irreducible decay is given by the internal conversion decay $\mu^+ \to e^+e^-e^+\nu_\mu\bar{\nu}_e$ which mimics a $\mu^+ \to e^+e^-e^+$ decay since the neutrinos can not be detected by the Mu3e detector. Its BR is $(3.4 \pm 0.4) \times 10^{-5}$ [10]. To discriminate the two decays, one uses that the neutrinos carry away momentum, so Eq. (1) does not hold for the visible particles. To detect this missing momentum the detector needs a momentum resolution of at least of 1 MeV in its final phase [2].

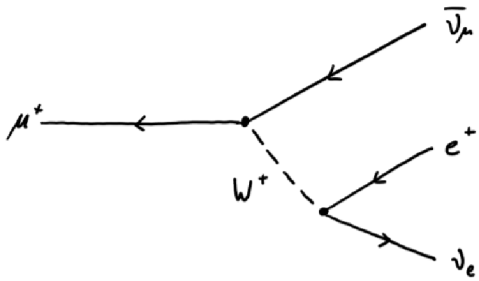

Figure 5: Michel decay

3.2.2 Accidental background

The accidental background is given by events where electrons from different decays are wrongly classified as a three electron event. The main decay mode of the muon with a BR of almost 1 is the Michel decay $\mu^+ \to e^+\bar{\nu}_\mu\nu_e$ (Fig. 5) [10]. Therefore, two positrons from different Michel decays and an electron from Bhabha scattering might seem like a $\mu^+ \to e^+e^-e^+$ decay (Fig. 6a). Another possibility is an internal conversion decay with one undetected positron and a positron from Michel decay which might be wrongly classified as a $\mu^+ \to e^+e^-e^+$ decay (Fig. 6b). To find out if three electrons originate from the same decay and therefore identify accidental background events, a time resolution of 20 ns or better is required of the experiments pixel sensors [2].

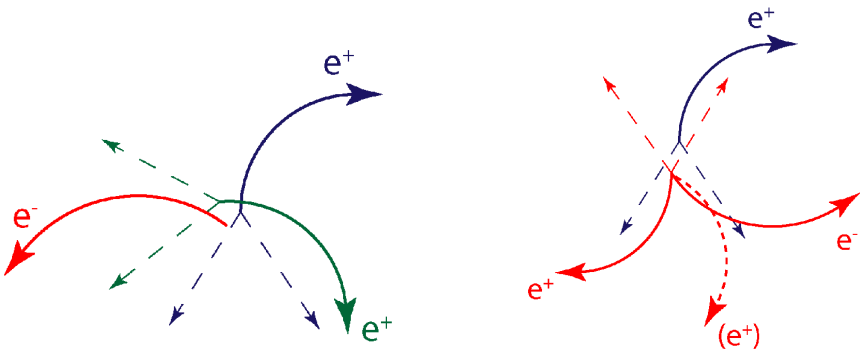

(a) from Bhabha scattering

(b) from internal conversion

Figure 6: Accidental background

3.3 The Mu3e detector

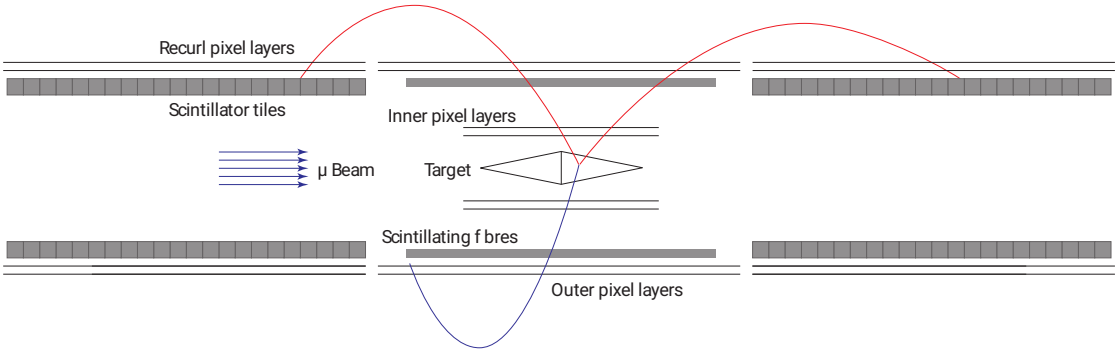

Figure 7: Mu3e Phase 1 detector. Taken from [4]

Fig. 7 is a scheme of the Phase 1 Mu3e detector. It is designed to have a high momentum and vertex resolution to discriminate signal to background. Along the beam pipe are three barrels: one main barrel in the middle and two recurl stations. The muon beam is directed at a 20 mm diameter double cone target in the centre of the main barrel where they are stopped and then decay.

The whole detector is inside an 1 T magnetic field. Therefore, the momentum of charged particles can be obtained from the curvature of the track of the particles. These tracks are reconstructed with help of the pixel sensors in the inner and outer pixel layers in the main barrel. However, the momentum resolution is mainly limited by scattering at the pixel layers. Therefore, there are the recurl stations which allow to detect the particles once more and further increase the momentum resolution. The charged particles follow bent paths which reenter the detector at the recurl stations. The outer layers of the recurl stations consist again of pixel sensors. This increases the momentum resolution especially since the effect of the scattering in the outer pixel layers is cancelled at first order at the recurl stations. At high rates it is necessary to have a good time resolution to reduce combinatorics

for the tracking. To achieve this resolution, a layer of scintillating fibres before the outer pixel layers of the main barrel and a layer of scintillating tiles in the recurl stations are included in the design.

4 Particle detection

To detect a particle one has to observe its interactions with the surrounding matter. The easiest way to do this is to measure the energy that a particle deposits on its way through a medium.

4.1 Heavy charged particles

The Bethe-Bloch formula (Eq. 3) describes the average energy deposition for heavy charged particles, i.e. charged particles with a mass greater than the mass of an electron. Those particles lose their energy mainly through ionisation. The mean energy loss per travelling length $\left\langle \frac{dE}{dx} \right\rangle$ is [10]:

$$\left\langle \frac{dE}{dx} \right\rangle = \frac{4\pi n z^2}{m_e c^2 \beta^2} \left(\frac{e^2}{4\pi\varepsilon_0} \right)^2 \left[\ln\left(\frac{2 m_e c^2 \beta^2}{I \cdot (1-\beta^2)} \right) - \beta^2 - \frac{\delta(\beta\gamma)}{2} \right] \tag{3}$$

Here $\beta = \frac{v}{c}$ is the relativistic velocity of the particle, z its charge number, n is the electron density of the material and I is its mean excitation. The term $\delta(\beta\gamma)$ compensates for the longitudinal compression of the electric field at high velocities. Furthermore m_e is the electron mass, c the speed of light in vacuum and ε_0 the vacuum permittivity.
In Fig. 8 the mean energy loss per travelling length $\left\langle \frac{dE}{dx} \right\rangle$ is depicted for different materials. For small relativistic velocities the interaction time increases leading to a higher energy loss. This effect is dominant for small velocities and causes a β^{-2}-like behaviour. For high velocities the relativistic effects get more important leading to a logarithmic increase of deposited energy. Particles with $\beta\gamma \approx 3$ are the particles with the least energy deposition per travelling length. They are called minimal ionizing particles.

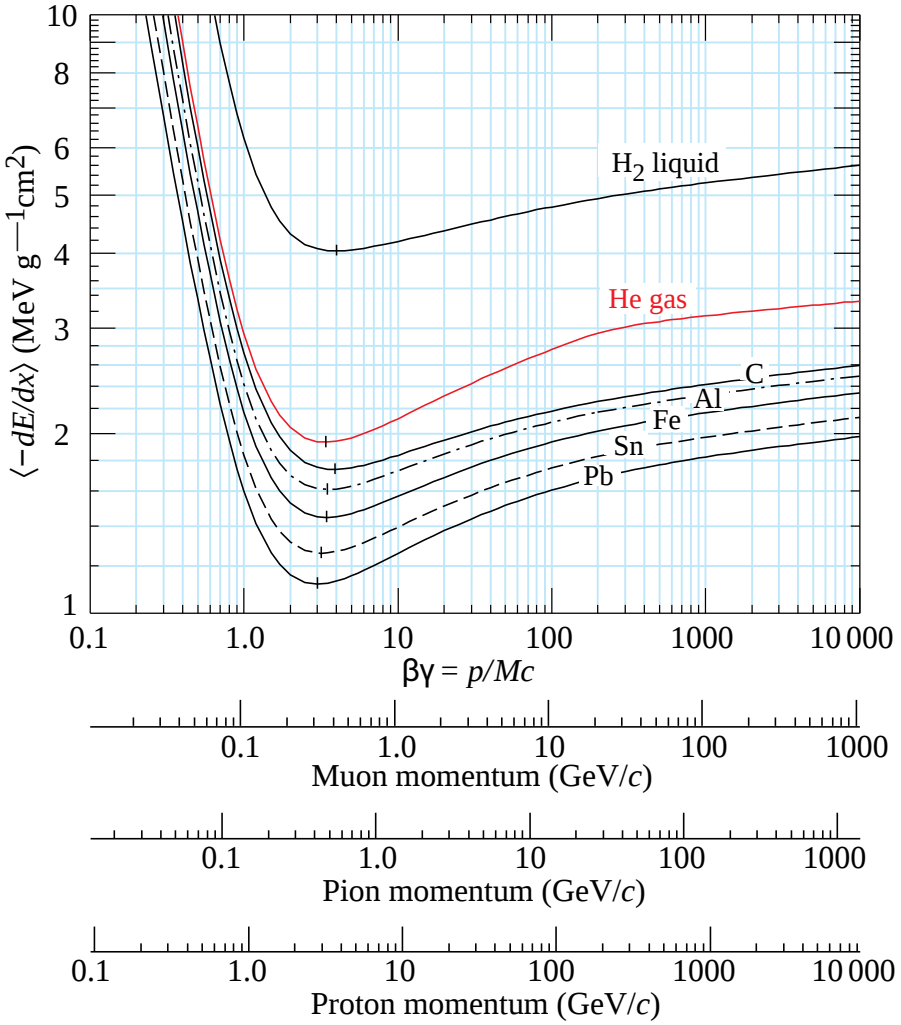

Figure 8: Mean energy loss per travelling length in different materials [10]

4.2 Electrons and positrons

For electrons and positrons, there are two more significant effects which are not covered by the Bethe-Bloch formula. First, due to their low mass they lose much more energy via bremsstrahlung. Second, the incident electrons are indistinguishable from the electrons of the material leading to repulsion. Incoming positrons, however, can annihilate with the electrons of the material. The Berger-Seltzer formula includes all these effects [11]:

$$-\left\langle \frac{dE}{dx} \right\rangle = \rho \frac{0.153536}{\beta^2} \frac{Z}{A} \left(B_0(T) - 2 \ln \left(\frac{I}{m_e c^2} \right) - \delta \right) \tag{4}$$

Here ρ is the material density and $\frac{Z}{A}$ is the ratio of protons to nucleons. $B_0(T)$ is the momentum dependent stopping power of the material which differs for electrons and positrons due to the effects described above. In Fig. 9 the mean energy loss per travelling length in silicon is plotted for electrons and positrons.

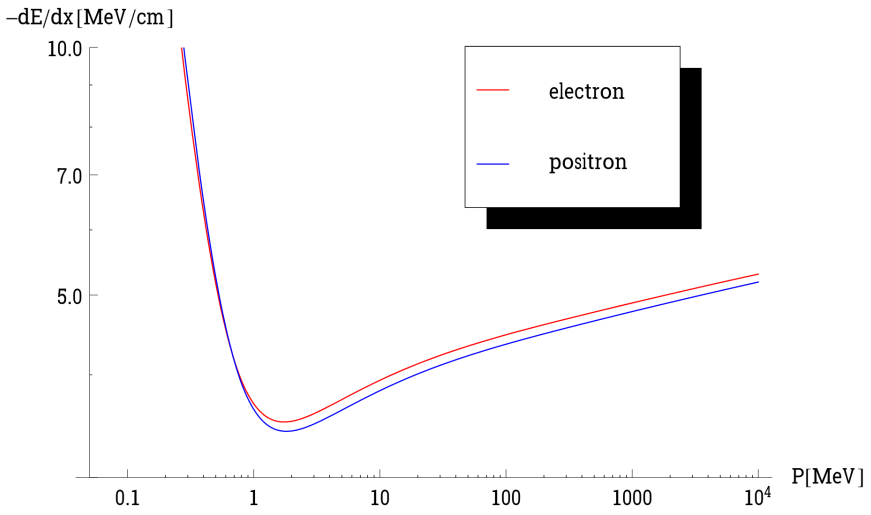

Figure 9: Mean energy loss per travelling length in silicon for electrons and positrons. Taken from [12] with data from [11]

4.3 Multiple Coulomb scattering

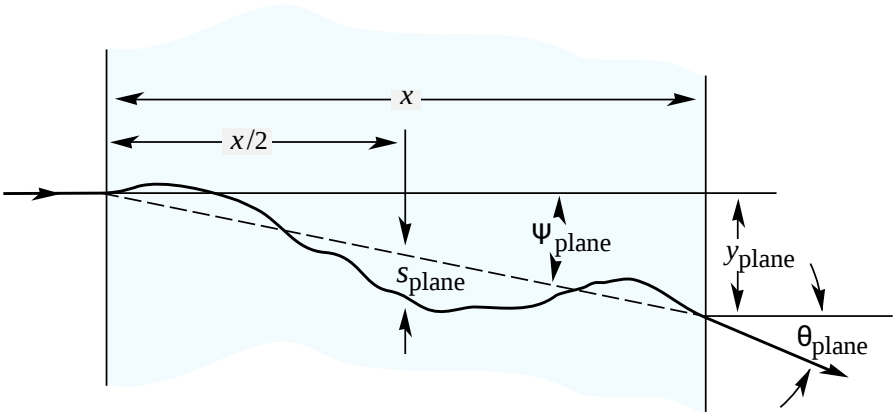

Figure 10: Multiple Coulomb scattering in the sensor. Taken from [10]

A particle travelling through a material will not only deposit energy, but also it will scatter multiple times in the electric field of the nuclei. The particle will leave the detector material at an angle Θ and an offset with respect to its original path (Fig. 10). For thin detectors the offset can be neglected. The angle Θ is distributed approximately Gaussian. The RMS can be obtained from the Highland Equation [10]:

$$\Theta_{rms} = \frac{13.6\,\text{MeV}}{\beta cp} z \sqrt{\frac{x}{X_0}} \left[1 + 0.038 \ln\left(\frac{x}{X_0}\right)\right] \tag{5}$$

Here z is the charge of the particle, p is its momentum and βc its velocity. X_0 is the radiation length.

The Multiple Coulomb scattering makes it harder to reconstruct the particle's original path and therefore limits the momentum resolution of the detector. This imposes tight material limits to the Mu3e detector system.

4.4 Scintillation light

A particle can excite some bound electrons to higher shells when travelling through a material. When they deexcite they emit scintillation light. This light can be measured to detect the particle.
There are two types of scintillators: inorganic scintillators are doped with other atoms which introduce additional energy states. Therefore, the scintillation light gets emitted at a frequency that the bulk material is transparent to.
Organic scintillators consist of two fluorescent substances where one substance causes a frequency shift of the light emitted by the other. The material is transparent to the frequency-shifted scintillation light. Organic scintillators exist as liquid and as plastic scintillators. They are well suited for timing measurements, because the excited states in organic scintillators usually have very short mean life spans.

5 Semiconductor physics

5.1 Semiconductors

If one describes the possible states of valence electrons in a solid body one finds that the physically possible states are ordered in certain energy intervals, the so called energy bands, whose exact range depends on the material. Charge transport is only possible in energy bands which are not completely filled. At $T = 0\,\mathrm{K}$ all electrons will occupy the lowest possible state, therefore filling up all states up to a certain energy, the Fermi energy. If this Fermi energy is in the middle of an energy band the material will be conductive. If, however, the Fermi energy is between two energy bands, the band above the Fermi energy, called the conduction band, is completely empty while the band below it, called the valence band, is completely filled meaning the material will act as an insulator.
However, for some materials, which are insulators at $0\,\mathrm{K}$, the band gap between valence and conduction band is so small that some electrons can be elevated from the valence band to the conduction band by thermal excitation at sufficiently high temperatures. These materials are called semiconductors. If one electron is excited to the conduction band it leaves a vacancy in the valence band. This vacancy is called hole and can for simplicity be viewed as a positive charge carrier. If one applies an external voltage to a semiconductur at a sufficiently high temperature

the electrons in the conduction band and the holes in the valence band contribute to a current that is higher the more electrons were excited.

5.2 Doping

It is possible to manipulate the band structure of a material by doping i.e. replacing some of its atoms by other atoms with a different amount of valence electrons. If one implants elements with more valence electrons some of those will be excited into the conduction band. This is called n-doping. If one implants elements with fewer valence electrons some of the electrons from the valence band might take the place of the missing electrons thereby creating "holes" in the valence band. This is called p-doping.

5.3 p-n-junction diode

If a p-doped material is brought in to contact with an n-doped one the density of electrons in the conduction band will be much higher in the n-doped material than in the p-doped material. This starts a diffusion process where electrons from the n-doped region wander into the p-doped one. Likewise the holes will diffuse from the p-doped region into the n-doped one. Without the diffusion process both regions would be neutral. With the diffusion process however, the amount of negative charge in the p-doped region increases as does the amount of positive charge in the n-doped region. Therefore, an electric field builds up which works against the diffusion process (Fig. 11). These two processes create a depletion zone of a certain width in which holes from the p-doped region and electrons from the n-doped region recombine. This means that this zone has almost no free charge carriers and is therefore not conductive. The natural width w can be calculated from the built-in voltage V_{bi} which results from the diffusion process as follows:

$$V_{bi} = \frac{kT}{e} \ln\left(\frac{n_A \cdot n_D}{n_i^2}\right) \tag{6}$$

$$w = \sqrt{\frac{2\varepsilon_0 \varepsilon V_{bi}}{e} \frac{n_A + n_D}{n_A \cdot n_D}} \tag{7}$$

Here n_A and n_D are the densities of donors respectively acceptors while n_i is the intrinsic density of charge carriers in the semiconducting material. kT is the product of Boltzmann constant and Temperature and e is the elementary charge. ε_0 is the vacuum permittivity and ε the relative permittivity.
If one applies an external voltage V_{ext} this effectively decreases the built-in voltage.

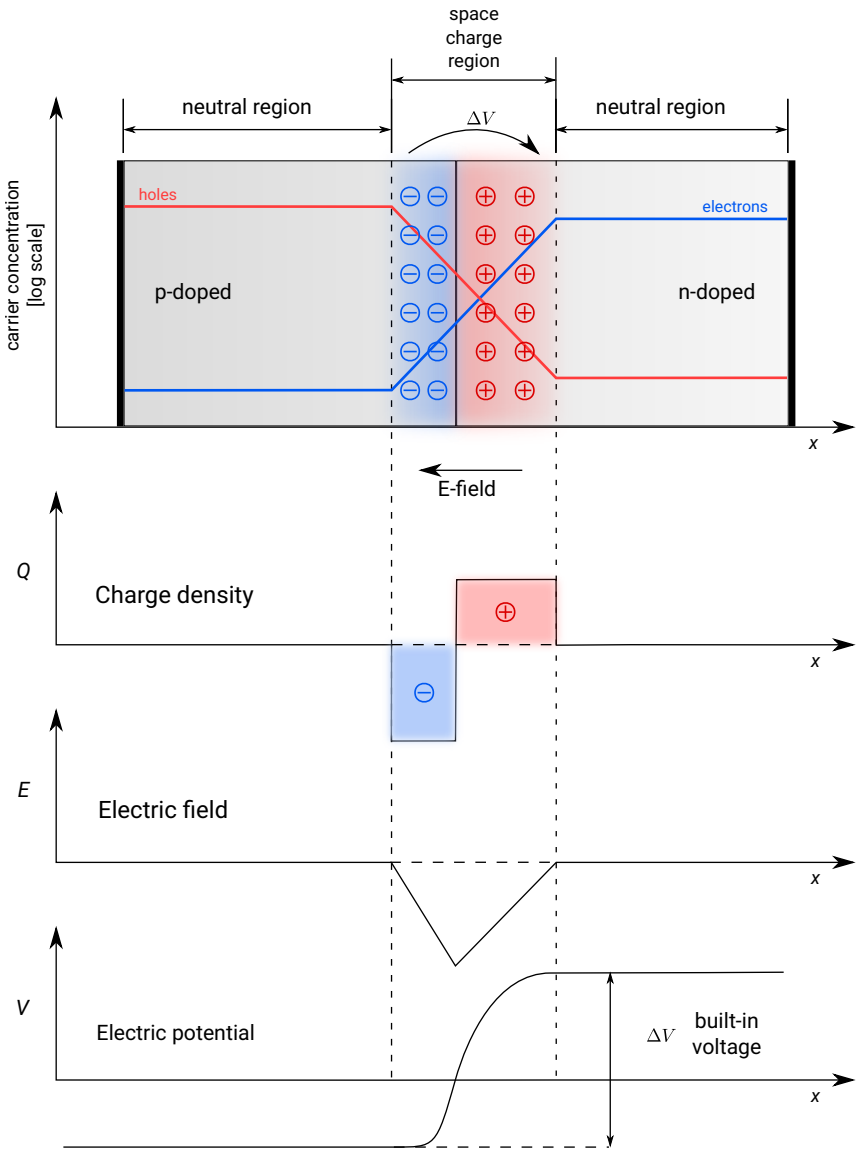

Figure 11: Schematic of a pn-junction. Taken from [13]

Then the width of the depletion zone is

$$w = \sqrt{\frac{2\varepsilon_0\varepsilon(V_{bi} - V_{ext})}{e}\frac{n_A + n_D}{n_A \cdot n_D}} \tag{8}$$

When the external voltage is bigger than the built-in voltage the depletion zone vanishes and the diode is conductive again. On the other hand one can increase the depletion zone by applying a negative voltage.

6 Semiconductor pixel sensors

When a charged particle or photon travels through a semiconductor it deposits parts of its energy by exciting electrons from the valence to the conducting band and therefore creating electron-hole-pairs. Usually the electron and the hole of them will diffuse and soon recombine. If the electron-hole-pair is created inside the depletion zone of a p-n-junction however, the electron and the hole are accelerated in opposite directions by the electric field. The electron hole pairs created by the particle form a small current which temporarily causes a slight discharge of the diode capacity. This can be picked up by mirror capacities and a charge sensitive amplifier to gain a measurable analogue signal
A pixel sensor consists of many of these diodes ordered in a matrix such that the position of a particle hitting the sensor can be determined. The general principle of the detection is the same for all pixel sensors. However, the way the charge is collected and the readout process vary.

6.1 Hybrid pixel detectors

For hybrid pixel detectors the diodes are read out with a separate readout chip. For each pixel on the detector chip there is a readout cell on the readout chip that is connected to the diode with a bump-bond. The charge collection is accelerated by applying a high voltage which increases the depleted region and also the electric field in it. The separate chip makes it easy to apply the high voltage to the diodes without it interfering with the readout process.

6.2 Monolithic Active Pixel Sensors

For applications where material budget is critical Monolithic Active Pixel Sensors (MAPS) have been developed. In contrast to the hybrid pixel sensors with one chip only for readout and the bump bonds which typically have rather short radiation lengths MAPS use only one chip for both signal generation and readout. The readout cell is on the same chip directly above the pixel diode.
MAPS can be produced using commercial available technology which makes them cheap in comparison to the hybrid pixel sensors. However, in conventional MAPS designs no high voltage can be applied. Therefore, the charge is collected through diffusion which is in the order of microseconds while charge collection via drift happens on the nanoseconds time scale.

6.3 High-Voltage Monolithic Active Pixel Sensors

High-Voltage Monolithic Active Pixel Sensors (HV-MAPS) improve the charge collection of MAPS by applying a high voltage to each diode, therefore being able to collect charges via drift. For each pixel a deep n-well forms the diode together with the p-substrate (Fig. 12). The pixel electronics is embedded in the n-well allowing it to function without interference from the other pixels.

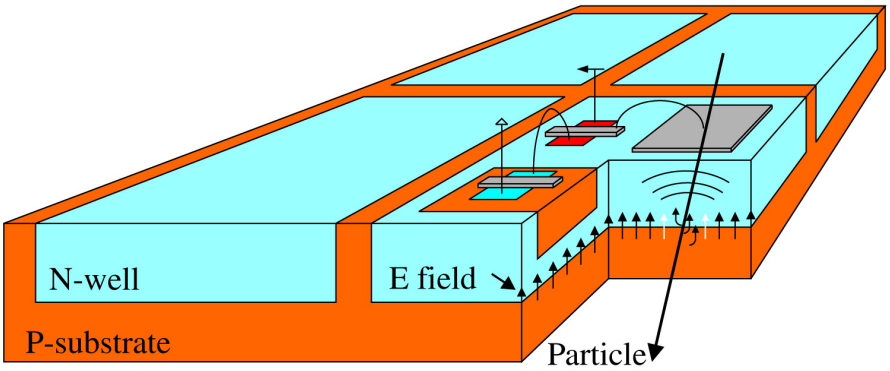

Figure 12: Basic scheme of the HV-MAPS technology [14]

Part II

Setup

7 MuPix10 sensor

For the Mu3e experiment a series of HV-MAPS sensors, the MuPix series, is developed to achieve good time resolutions while maintaining a low material budget. The MuPix10 is the first full-scale prototype for the Mu3e experiment. Its total size is $20.66 \times 23.18\,\mathrm{mm}^2$ and it contains a pixel matrix with 250 rows and 256 columns (Fig. 13). Each pixel has a total size of $80 \times 80\,\mu\mathrm{m}^2$. The remaining space of the sensor is filled with the digital periphery which contains the timestamp generation and the readout circuitry. The pixels are organised in double columns which are two adjacent columns which share for example readout buffers.
Many resistances, voltages and capacitances on the chip can be adjusted by digital to analogue converters (DACs) either for the whole sensor or individually for each pixel.
Fig. 14 depicts the readout concept of the MuPix10. The signal is generated either in the diode by a particle traversing through the pixel or by an external injection pulse. The generated charge is collected by a feedback capacity and amplified by a

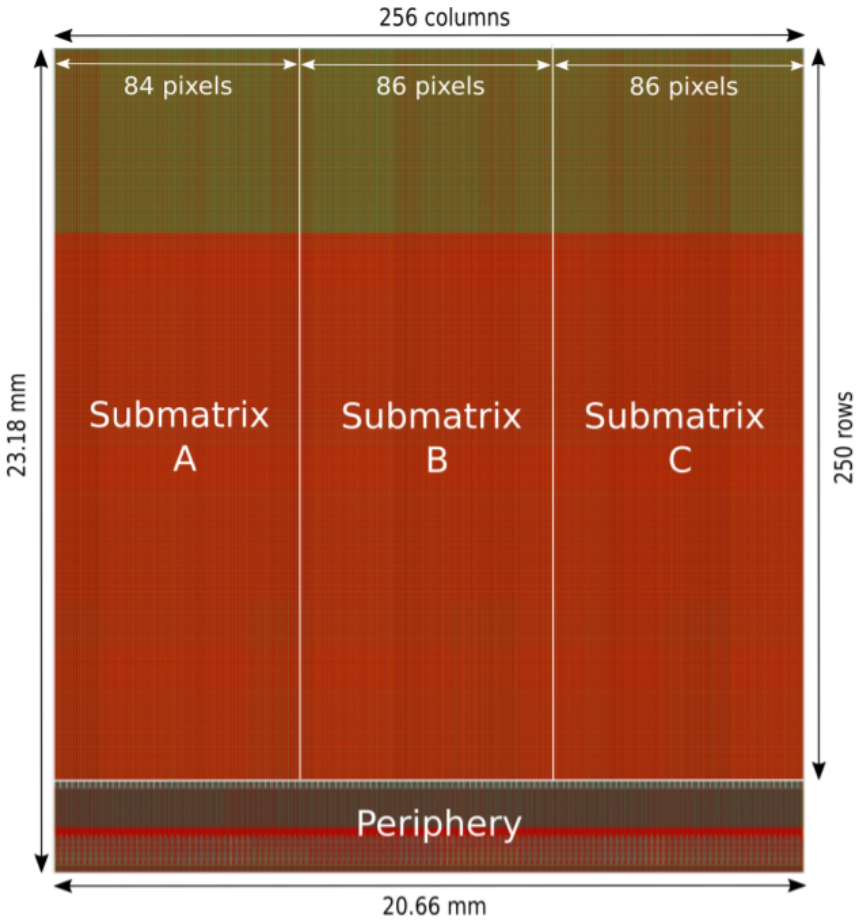

Figure 13: MuPix10 layout taken from [9]

charge sensitive amplifier (CSA). Subsequently the signal is capacitively coupled to the baseline of the pixel (BlPix) and driven to the digital periphery. The periphery is decoupled from the pixel cells. Hence, the signal is modulated onto the baseline of the periphery (BlDig). There the signal gets discriminated at a certain threshold voltage to get a digital signal. The MuPix10 has two comparators per pixel which allows two compare the signal with two different threshold levels. However, in this thesis only comparator 2 is used. The threshold voltage for comparator 2 is called ThLow.

An edge detector generates timestamps from the comparator output.

Timestamp 1 (Ts1) is generated as soon as the comparator detects the signal exceeding the threshold. Timestamp 2 (Ts2) is generated when it is below the threshold again. Both timestamps have limited amount of bits. Their granularity can be controlled by the two DACs $ck1$ and $ck2$. Ts1 is 11 bits long and its value is increased by one for every $(ck1 + 1)$ ticks of the main clock provided to the sensor. Ts2 has a size of 5 bits and increases every $(ck2 + 1)$ ticks of the main clock. In this thesis a frequency of 125 MHz is used for the main clock.

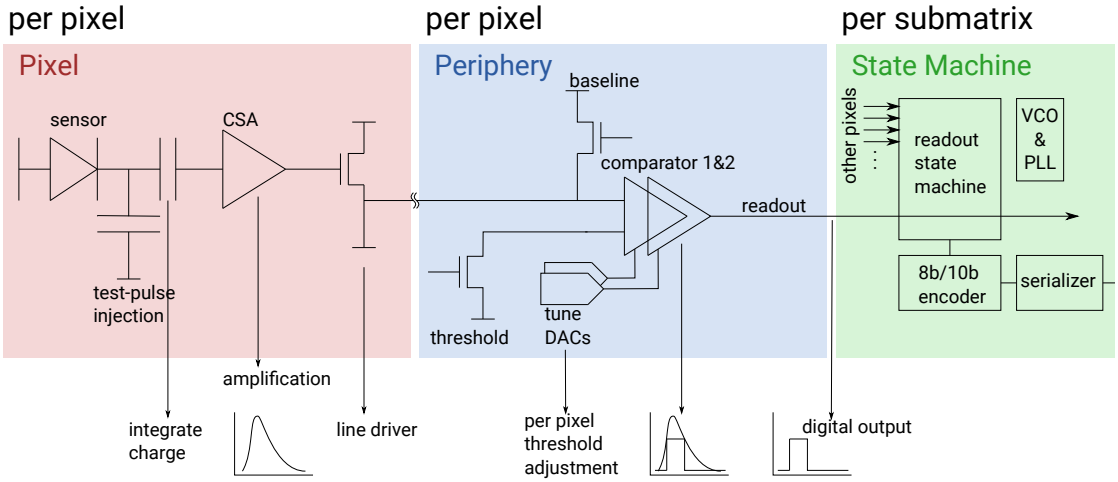

Figure 14: Readout concept of the MuPix10 [15]

In the last step of the readout chain these timestamps are sent out of the sensor. The outgoing data is usually processed by a field programmable gate array (FPGA) and can later be analysed by software. In each readout cycle only one hit per double column can be read out. If multiple hits are registered in the same readout frame they are buffered and read out in one of the following frames.
The chip is powered by the supply voltages VDDA for the analogue part, VDDD for the digital periphery and VSSA as a supply voltage exclusively for the amplifiers.

7.1 Time resolution

The time between a particle hitting the pixel and Ts1 is called the latency of a hit. In an ideal sensor the latency would be the same for every hit which would allow to always deduce the exact time of a hit. However, in a real sensor different effects cause a dispersion of the latency so there is always a difference between the time of a hit and the best estimate for it based on the sensor information. The time resolution σ is defined such that for 68 % of the hits the estimate falls into an interval of $\pm\sigma$ around the actual time of the hit. Therefore, if the latency dispersion is a Gaussian the time resolution is the σ of the Gaussian. This is depicted in Fig. 15.

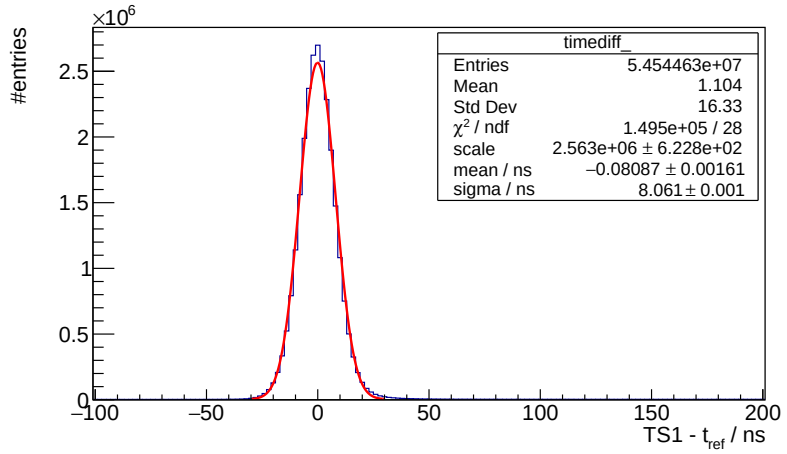

Figure 15: The latency dispersion is a Gaussian if Ts1 is corrected for various effects as described in Section 9

7.2 Time-walk and Time over Threshold

For the MuPix8 one of the main contributions to the time resolution is time-walk [16].

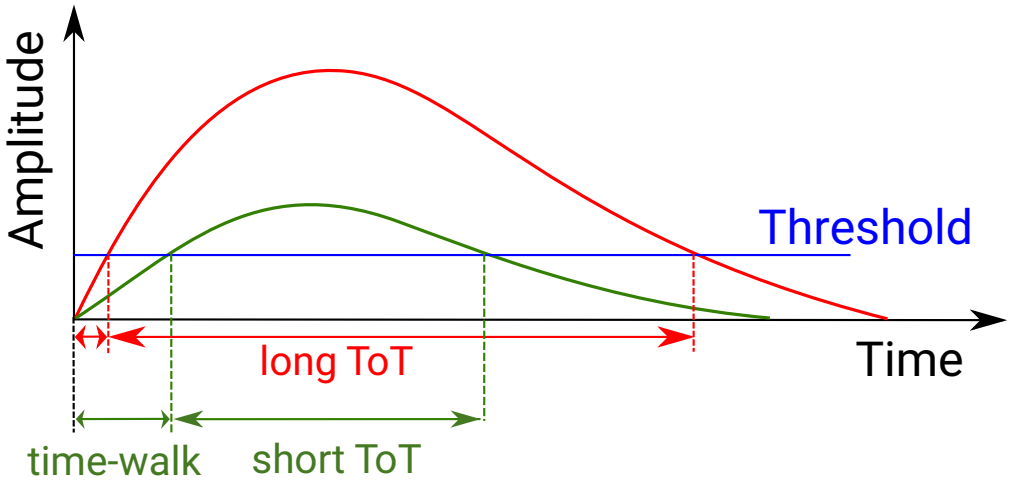

Figure 16: Concept of time-walk. Signals with longer ToT in general have a shorter time-walk. Adapted from [16]

When charge is deposited in the diode or injected it takes some time for the amplified signal to build up to the level where it exceeds the threshold (Fig. 16). This time is called the time-walk. The more charge is deposited, the higher is the signal amplitude and the steepness of the rising edge of the signal. Also the time over threshold (ToT) which is the time between Ts1 and Ts2 increases with the deposited charge. The correlation between time-walk and the ToT can be used to correct Ts1 such that it is closer to the actual time of the particle hit which improves the time resolution.

For lower threshold levels the time-walk gets less as the signal needs less time to

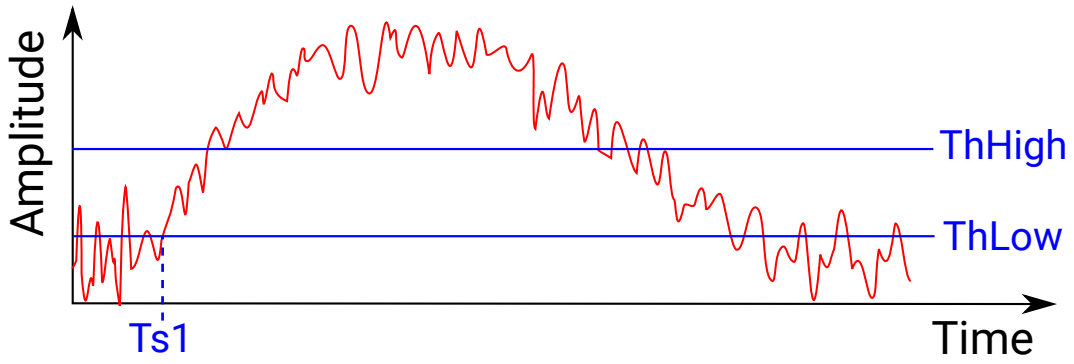

Figure 17: Concept of two-threshold mode. Adapted from [16]

exceed the threshold. Therefore, the time resolution is expected to improve for lower threshold levels. However, the minimum threshold is limited by the noise on the baseline because for threshold levels below the noise level the pixel would continuously detect false hits. To circumvent this effect the two-threshold mode can be used. For this ThLow is chosen in the noise level, but the other comparators threshold ThHigh is chosen above the noise level (Fig. 17). A hit is only registered if the signal exceeds ThHigh. That means that only pulses which are above the noise level are detected, but Ts1 is set by a threshold which is closer to the baseline than the noise level would usually allow. Two-threshold mode was one time-walk correction method tested with the MuPix8 [16]. In this thesis, however, only time-walk correction based on ToT will be investigated.

7.3 Pulse shaping

The amount of time-walk and the exact correlation between ToT and time-walk depends on the signal shaping. The four DACs controlling the signal shape are the amplifier DACs VNPix, VNFollPix, VNFB, BLResPix which are described in the following.

VNPix VNPix controls the current source of the amplifier. At previous MuPix sensors it had a large impact on the pulses amplitude and rising edge [16].

VNFB VNFB is the linear feedback of the amplifier. It can be used to adjust the ToT range. The influence of VNFB on the ToT is measured in Section 10.3.

VNFollPix VNFollPix is the internal feedback driver.

BlResPix BlResPix is a resistance which acts as a high pass together with the capacitive coupling of the signal to the pixel baseline BlPix. It also can be used

to adjust the ToT range. The influence of BlResPix on the ToT is measured in Section 10.3 as well.

7.4 Time over threshold cap

To ensure that no hit is read out before Ts2 is set and at the same time maintain approximate data chronology a new feature has been introduced with the MuPix10: The time over threshold cap (ToT-cap). The ToT-cap circuitry is shown in Fig. 18. When a hit is registered and Ts1 is set the readout of the hit is disabled. At the same time the condensator C_{del} is charged up by a constant current which can be adjusted with VPTimerDel. When the voltage of the condensator exceeds a certain threshold voltage defined by the DAC VNTimerDel the hit readout is enabled again. Additionally Ts2 is set if it was not set earlier. In case of large signals this means that Ts2 is set before the signal has decayed below the threshold. Hence, there is a maximum ToT which can not be exceeded. As this only affects large signals which suffer not much from time-walk, this procedure should not worsen the time resolution significantly while allowing almost constant readout times for every hit. In principle, the maximum ToT that can be reached is constant, but it might differ between pixels due to production variations.

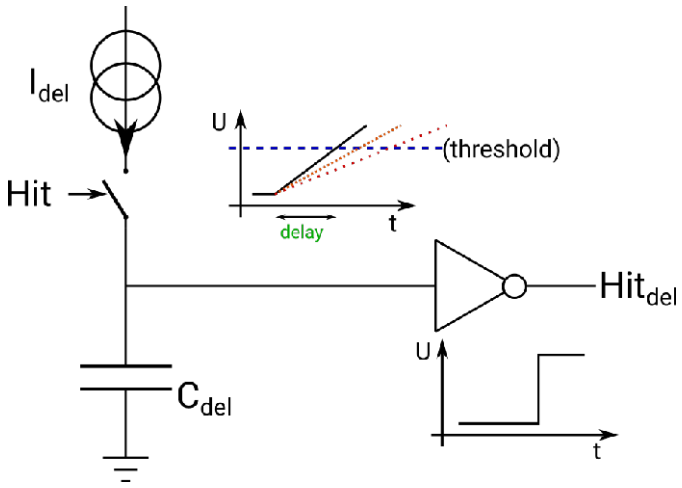

Figure 18: ToT-cap circuitry. Reset circuit is not shown. [17]

7.5 Transmission lines

Each pixel is connected to a readout cell in the digital periphery with its own transmission line. The transmission lines couple capacitively to each other. This causes two undesirable effects. A signal can induce a smaller signal in a neighbouring transmission line. This is called transmission line crosstalk. Also the signal gets distorted which causes a delay, the so called transmission line delay. Together

with time-walk it is the main source of the latency between the time of a hit and the the timestamp of the hit.
The routing scheme of the Mupix10 is designed to minimize crosstalk. For this, the distance between two neighbouring lines has to be maximised and the shared distance of two neighbouring transmission lines has to be as small as possible. Two metal layers are used for the routing. Transmission lines on different metal layers are coated from each other, so they can not induce crosstalk in each other. This allows a routing scheme where the shared length of two neighbouring transmission lines is always $\frac{1}{4}$ of the matrix length (Fig. 19). For this the pixel matrix is divided into four sectors of about 60 rows each and transmission lines in the same sector have similar length. The sector borders are slightly different for odd and even columns (Table 1). Therefore, the transmission line delay is expected to be similar for pixels in the same sector. Another advantage of the routing scheme is that its distinctive pattern allows to identify crosstalk [17].

	odd columns	even columns
Sector 1	0 - 59	0 - 61
Sector 2	60 - 118	62 - 124
Sector 3	119 - 184	125 - 186
Sector 4	185 - 249	187 - 249

Table 1: Sector border rows for odd and even columns

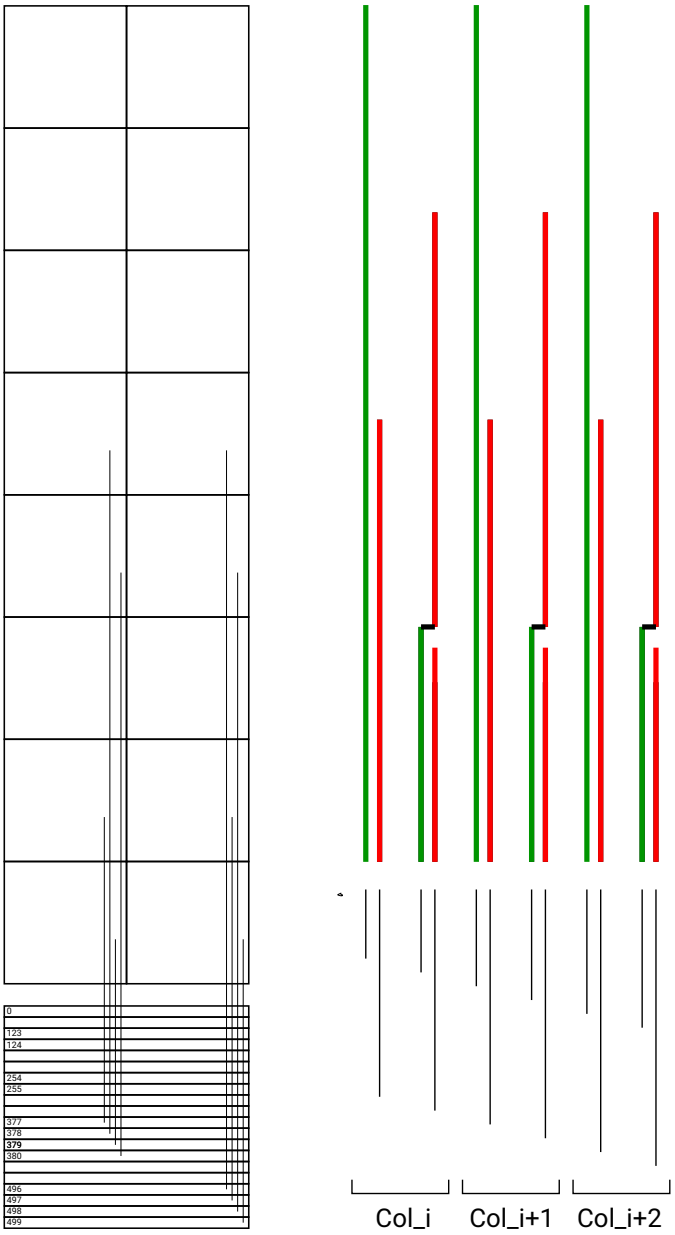

(a) Pixel routing. 2 metal layers with 256 and 244 lines respectively. (b) Metal layer usage. Red: metal 5, Green: metal 4.

Figure 19: Routing scheme of the MuPix10 [17]

7.6 Signal injection, hitbus and AmpOut

For testing purposes, the signals of selected pixels can be accessed and measured directly: the AmpOut signal is the signal after the amplifier. It is only available for pixels in row 0. The hitbus is available for every double column. It is implemented as the logical OR of the comparator 2 outputs of all pixels in the double column. It is possible to artificially generate a signal by injecting charge into a pixel. This is done by first charging a capacity which is connected in parallel to the pixel diode and then suddenly discharging it. The sudden discharge imitates a signal from a real particle hit. It is possible to control the voltage, duration and the frequency

of the injection. While injecting into a pixel, however, also the corresponding pixel of the double column in the same row is injected into. Two such pixels are referred to as a double pixel.

8 Setup

The MuPix10 is bonded onto a custom Printed Circuit Board (PCB), the so called insert (Fig. 20). It is connected to the motherboard PCB (Fig. 21a) and can be easily switched out for an insert with another sensor.
The insert provides test points which allow to measure certain voltages and signals as for example BLPix, BLDig, ThLow and the AmpOut.
The voltages and clocks needed by the sensor are generated on the motherboard PCB and reach the sensor via an edgeconnector and the insert. The supply voltages VDDA, VSSA and VDDD are generated by a HAMEG HMP4040 power supply which is directly connected to the insert. The high voltage is connected to the PCB via an SMA cable. Two other SMA connections supply the motherboard with its supply voltage. The sensor configuration and readout is done from an FPGA which is connected to the motherboard with an SCSI connector. The FPGA itself is controlled by a computer with a costum graphical user interface.
On the motherboard there are two LEMO connectors which allow to connect injection signal and hitbus to an oscilloscope. Here, an Tektronix DPO 7245C digital oscilloscope [18] is used. AmpOut and injection are terminated with 1 MΩ. The hitbus is terminated with 50 Ω. To filter high frequency noise the bandwidth is set to 20 MHz for all channels.
The motherboard PCB is mounted on top of a reference layer PCB carrying a scintillating tile (Fig. 21b) such that the sensor is directly above the scintillating tile. The reference layer PCB is connected to the FPGA with a LEMO cable. The

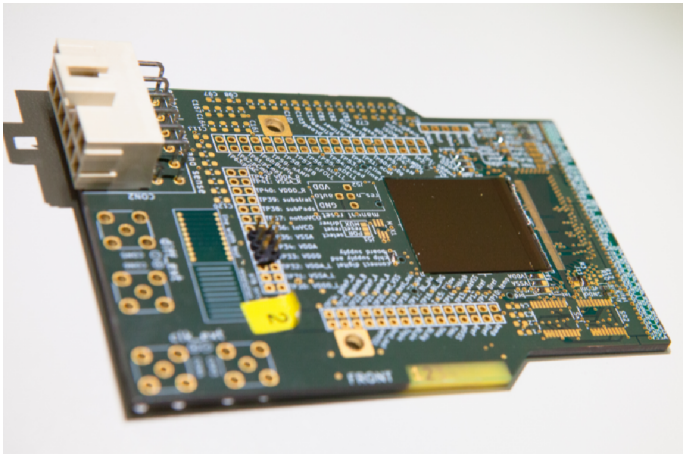

Figure 20: Mupix10 insert with bonded sensor [9]

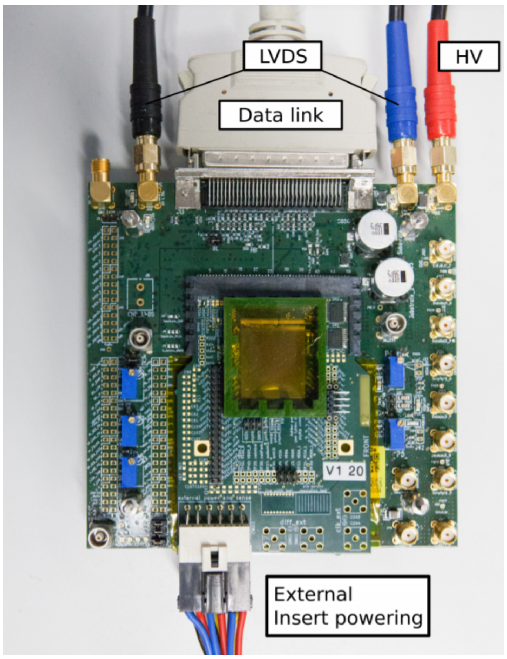

(a) Motherboard PCB with insert [9]

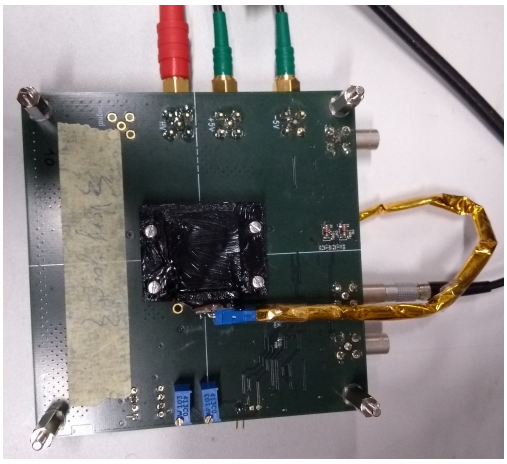

(b) Tileboard PCB with scintillating tile

Figure 21: Motherboard and tileboard PCB

tiles time resolution is about 1.4 ns [16] and thus significantly smaller than the expected time resolution of the MuPix10.
For measurements without injection a Strontium 90 (Sr90) radioactive source is placed above tileboard and motherboard PCB of them as depicted in Fig. 22.

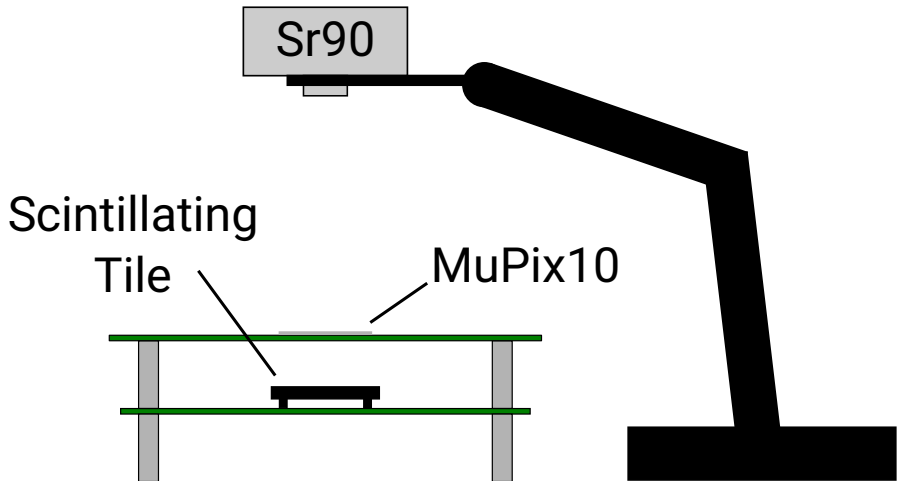

Figure 22: Schematic setup with a Sr90 source

9 Measurement methods

There are two main measurement methods used in this thesis. The first one uses injected pulses recorded by an oscilloscope, while the second one uses a Sr90 source to generate hits from real particles and then analyzes the digital data from the sensor.
For the analysis there are two approaches: normal analysis and single pixel analysis. This section will describe both measurement methods and their respective approaches to analysis.

9.1 Oscilloscope measurements with injection

The first type of measurement consists of injecting charge into the amplifier circuits of a double pixel and then monitoring with the oscilloscope the hitbus, injection and, if available, the AmpOut signal. The measurements are carried out by the oscilloscope's internal software. The oscilloscope triggers on both the injection signal and the hitbus to make sure that only acquisitions with a proper hitbus response are included in the measurements. A detailed description of the oscilloscope and its internal software can be found in the user manual [18]. The following variables will be measured:

ToT The ToT corresponds to the width of the hitbus signal (Section 10.2). The hitbus is active low, which means that the hitbus voltage is smaller when the signal is over the threshold than when it is below. Therefore, a reference level is set at 50 % the distance between low and high level of the signal. The hitbus width is then measured between the hitbus signal crosses the reference level down and up.

Latency The latency is the time between the injection signal and the hitbus signal. It is measured from the 50 % reference level of the falling edge of the injection to the 50 % reference level of the falling edge of the hitbus.

Time resolution After a series of injection signals is recorded the latency distribution is collected in a histogram. This distribution follows a gaussion and its standard deviation is the time resolution.

All variables are measured multiple times and the mean and the standard deviation of those measurements is used as measured value and error respectively.

9.2 Measurements with strontium source

As an alternative to the measurements with oscilloscope the hit data from a Sr90 source can be analysed. For this the Sr90 source is placed over the chip and the reference tile as described in Section 8. The hit data from the Mupix10 and the reference time stamps are collected by the DAQ and stored by the control software. The data is then processed for the analysis as follows.
The DAQ saves the data in so called time frames which correspond to the readout cycles. Since it can only read out one hit per column in a readout cycle, sometimes a hit is not stored into the same time frame as the corresponding reference time event. Therefore, a series of frames is merged into a single frame until an empty frame occurs.
A particle can activate multiple adjacent pixels either because it traverses through all of them or because of charge sharing. Therefore, hits within the same merged time frame which are adjacent to each other are combined into one cluster. The clusters timestamps Ts1 and Ts2 are taken from the earliest hit in the cluster. The cluster position is the barycenter of all the hits constituting the cluster.
In the analysis the hits from the scintillating tile are used as reference time events. Usually a frame contains one reference hit and multiple sensor hits. Because of this it is unfeasible to match with high precision which sensor hit must be associated with a reference time event. Therefore, all combinations of one cluster and one reference time event in the same merged time frame are processed. This gives rise to a combinatorial background of combinations which are processed although they do not originate from the same particle.

ToT The ToT can be calculated from the timestamps as follows:

$$ToT = [(ck2 + 1)Ts_2 - (ck1 + 1)Ts_1]\, t_{base}$$

Here t_{base} is the period of main clock provided to the sensor. Throughout this thesis, a 8 ns clock is used. $ck1$ is always 0 meaning that Ts1 is recorded with an 8 ns clock cycle. $ck2$, instead, is set to 31, so that ToTs up to about 8 µs can be seen.
The formula for the ToT given above is simplified. In the analysis software a more complex formula is applied that accounts for the different ranges of the timestamps due to their limited amount of bits.

Latency The latency of a single hit is simply the difference between the timestamp of the hit Ts1 and the timestamp of the tile, used as reference timestamp. Depending on the analysis performed, the hit data can be divided into specific

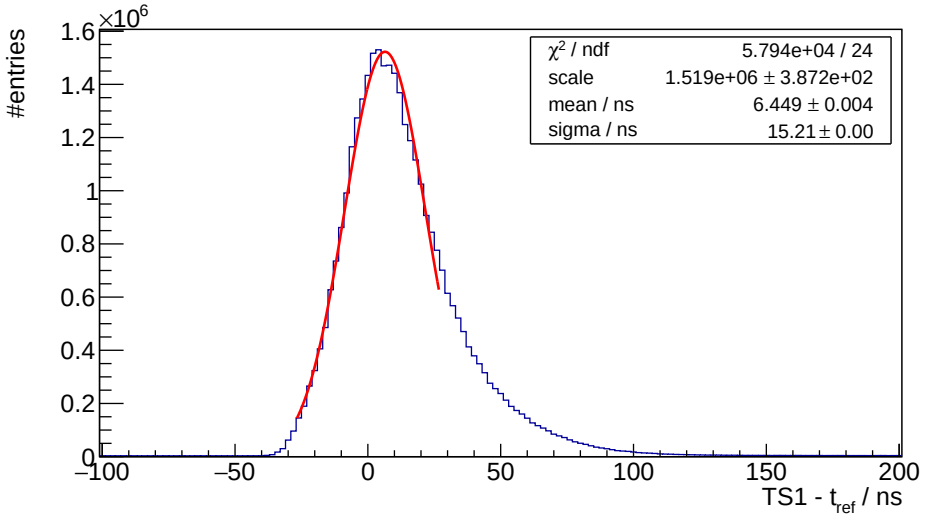

Figure 23: Latency dispersion calculated from the raw data

regions of the sensor. Typical regions are the whole sensor, one column, one row and a single pixel. In each analysis, the latencies of all hits in the region are histogramed. The resulting plot is the latency dispersion due to transmission line delay and time-walk. It is mostly Gaussian but high time-walk at hits with a small ToT causes a tail.
The latency can be retrieved from the histogram either by taking a weighted mean or with a gauss fit (Fig. 23).

Time resolution To get the time resolution a Gaussian is fitted to the interval of ±30ns around the maximum bin in the latency histogram. The time resolution is the σ of this Gaussian. The Gaussian includes a background term for the combinatorial background. The timestamps of each background event are uncorrelated. Therefore, the background forms a triangular background with the only free parameter being the amplitude of the triangle (Fig. 24).

$$f_{background}(\triangle t) = A \times (T - |\triangle t|)$$

Here $T = 2^{11} \cdot t_{base}$ is the range of $Ts1$ in nanoseconds and $\triangle t = Ts1 - Ts_{ref}$ the latency.
The amplitude of the combinatorial background is calculated from the number of hits I in the first $\frac{7}{8}$ of the latency histogram using the following relation:

$$A = \frac{2I}{\frac{7}{8}T} \cdot \frac{8}{7} \tag{9}$$

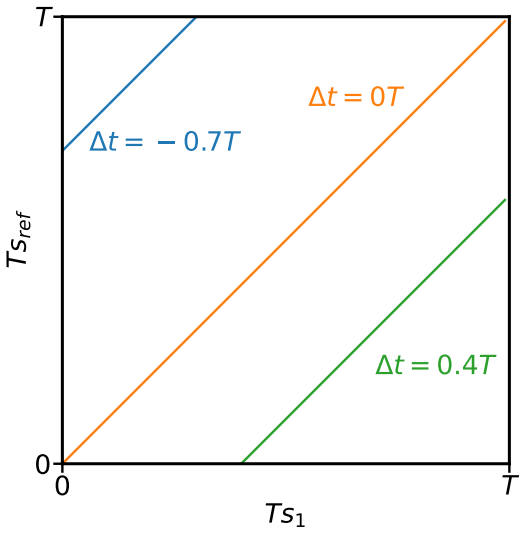

Figure 24: Each event of the combinatorial background will be a random point in this plot. The probability of combinatorial background with a special $\triangle t$ is given by the area of the line $Ts_{ref} = Ts_1 - \triangle t$.

Therefore, the full fit function including the combinatorial background is:

$$\begin{aligned} f_{fit}(\triangle t) &= f_{Gaussian}(\triangle t,\ \mu, \sigma, s) + f_{background}(\triangle t) \\ &= \frac{s}{\sqrt{2\pi\sigma^2}} \exp\left(-\frac{(\triangle t - \mu)^2}{2\sigma^2}\right) + A \times (T - |\triangle t|) \end{aligned}$$

Since the amplitude of the background is fixed by Eq. (9) the only free parameters of the fit are the mean latency μ, the time resolution σ and the scale of the Gaussian s.

The time resolution depends on the choice of the interval that is fitted. If the fitting range is increased typically the time resolution gets worse. Therefore, to estimate the systematic error of the time resolution the fit is done for 15 different intervals from ±20ns to ±150ns around the maximum bin. The error is then the standard deviation of the time resolutions obtained this way. The statistical error can be retrieved from the Gaussian fit but is negligible compared to the systematic error.

9.2.1 Corrections

In the analysis different corrections are applied to the data. Some cuts and corrections are related to the data quality and are applied by default in every analysis. These are the region of interest cut, the run correction and the crosstalk filter. Since they do not affect the time resolution, the data after this pre-processing phase is considered "uncorrected" data.

The time-walk correction and the delay correction correct for the effect of the time-walk and the row delay respectively. Their goal is to improve the time resolution and throughout this thesis each result is labeled "time-walk corrected" and/or "delay" corrected, depending on which of them have been applied. If both of them have been applied the resulting time resolution is called corrected time resolution. In the rest of this section the different cuts and corrections, both default and analysis-specific, are described.

Region of interest The pixels at the edges have different capacitances than the rest of the pixel matrix. Also the 24 rightmost columns have no proper Ts2. Therefore, only the hits in pixels of the so called region of interest (ROI) are used for the analysis. The ROI is an rectangle from row 11 to 238 and column 11 to 238.

Run correction The DAQ saves the run data in chunks of about 300MB and each of these chunks is called a run. In each run the clock of the FPGA is synchronised with the clock supplied to the MuPix10, which runs at 125 MHz. The FPGA runs with a clock frequency of 500 MHz. Therefore, for each synchronisation there are four different phases which the two clocks can have relative to each other. To correct for this effects every hit is shifted by the mean delay of the run.

Crosstalk filter For some configurations of the chip, a high crosstalk rate can be observed (Section 7.5). A hit with high amplitude induces a much smaller signal in a neighbouring transmission line. Since the real hit has high amplitude it also has high ToT and little delay from time-walk. The induced signal has a small ToT but roughly the same latency as the real signal. In principle crosstalk hits can be filtered if one uses the routing scheme of the transmission lines to detect crosstalk patterns. However, this method of crosstalk filtering had not been implemented by the time the data for this thesis was collected. Therefore, a cut is applied filtering out those hits with low ToT and unusually small latency (Figs. 25a and 25b).

Time-walk correction The time-walk is an important source of latency which can be corrected using the correlation between ToT and the latency itself as follows. The ToT spectrum is divided into ToT slices and for every ToT slice the mean latency is calculated. Each hit is then corrected according to its ToT by this mean latency (Fig. 25c).

Delay correction The capacitive coupling of the transmission lines causes a delay and also distorts the original amplifier signal. To correct the delay caused

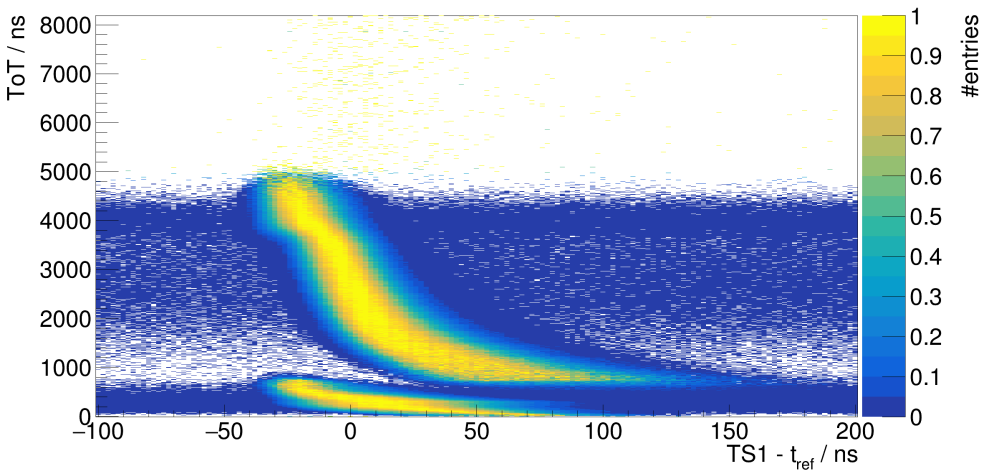

(a) uncorrected data but before crosstalk cut

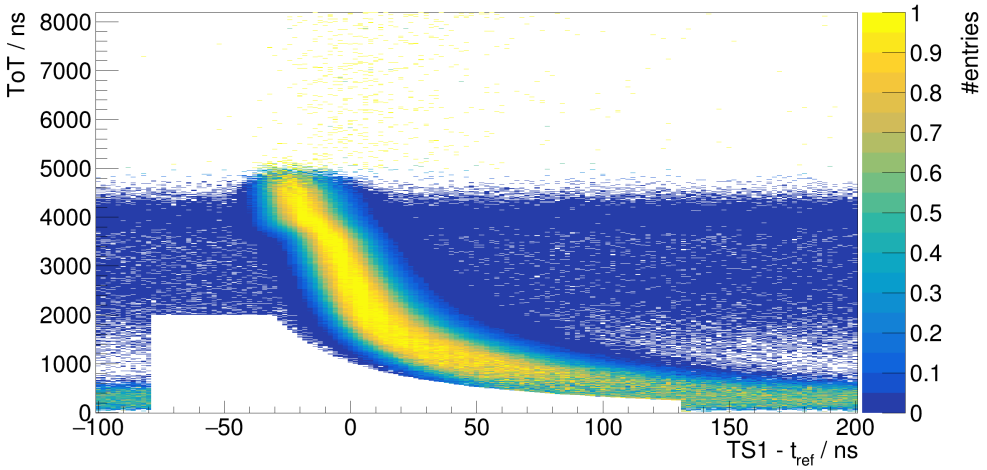

(b) uncorrected data after crosstalk cut

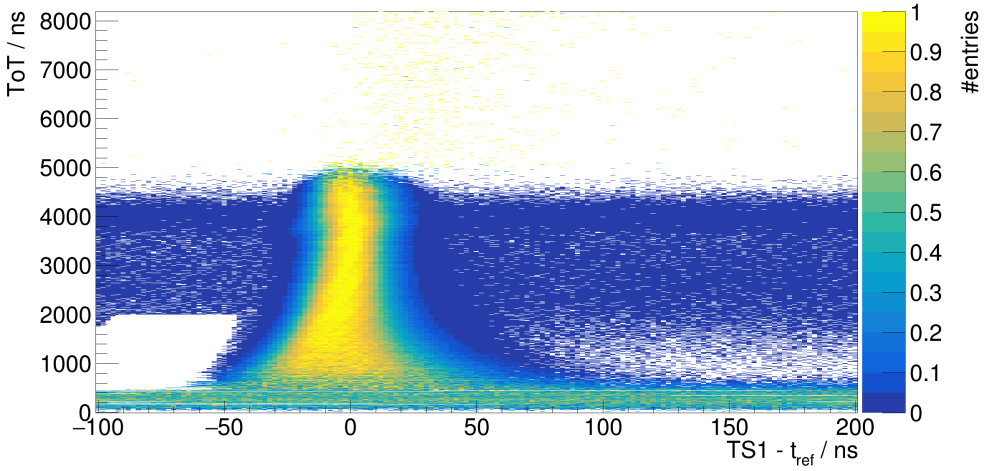

(c) time-walk corrected

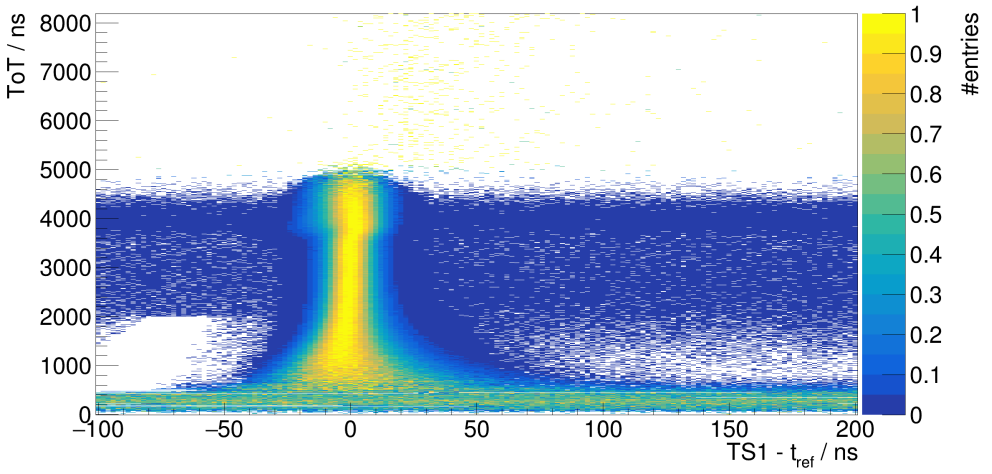

(d) time-walk and row delay corrected

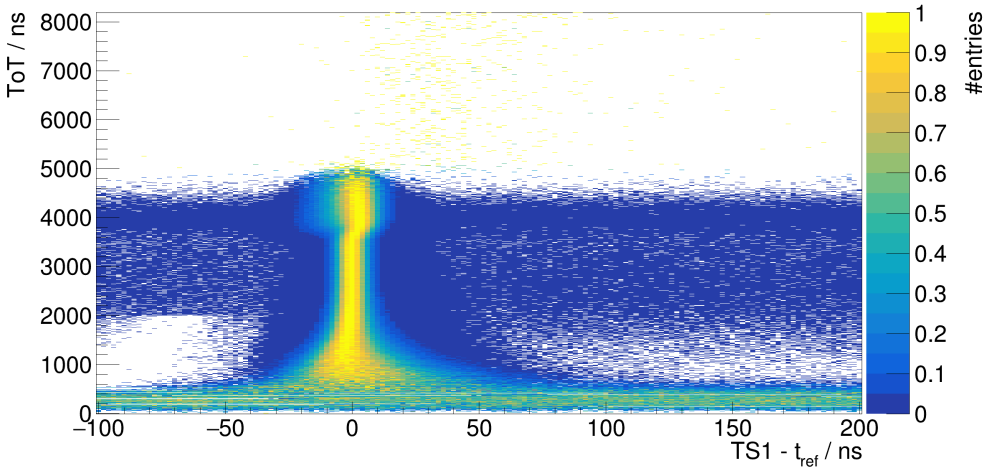

(e) time-walk and single pixel delay corrected

Figure 25: 2D distributions of latency versus ToT for all pixels in the ROI at different stages of the analysis. Each ToT slice has been normalised to 1.

by this effect there are two main methods: row delay correction and single pixel delay correction.

Single pixel delay correction

The simplest method to correct this delay is to correct each hit by the mean delay of its pixel. This delay is calculated by fitting a Gaussian to the pixel's latency distribution. Fig. 26 shows the delay map of the pixel before and after single pixel delay correction.

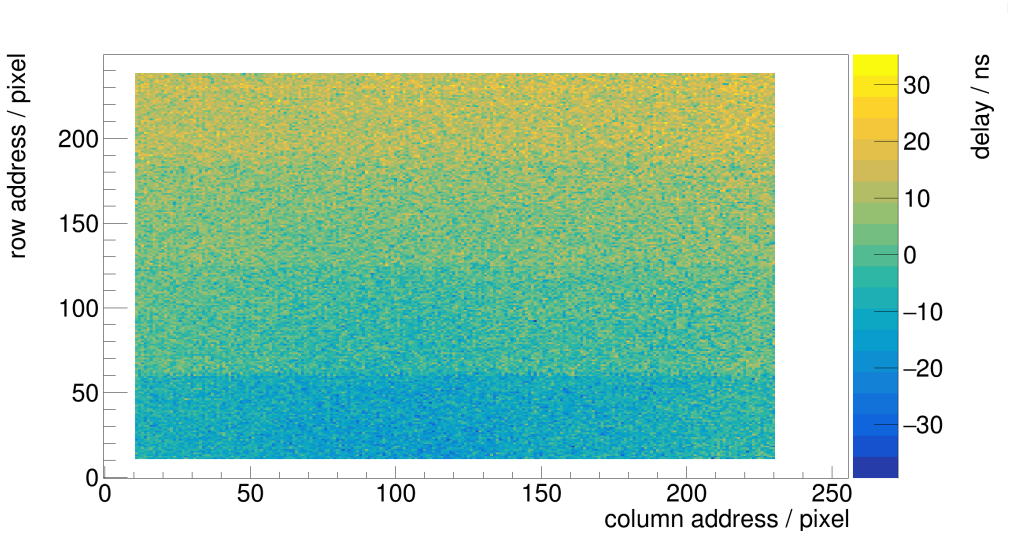

(a) Time-walk corrected

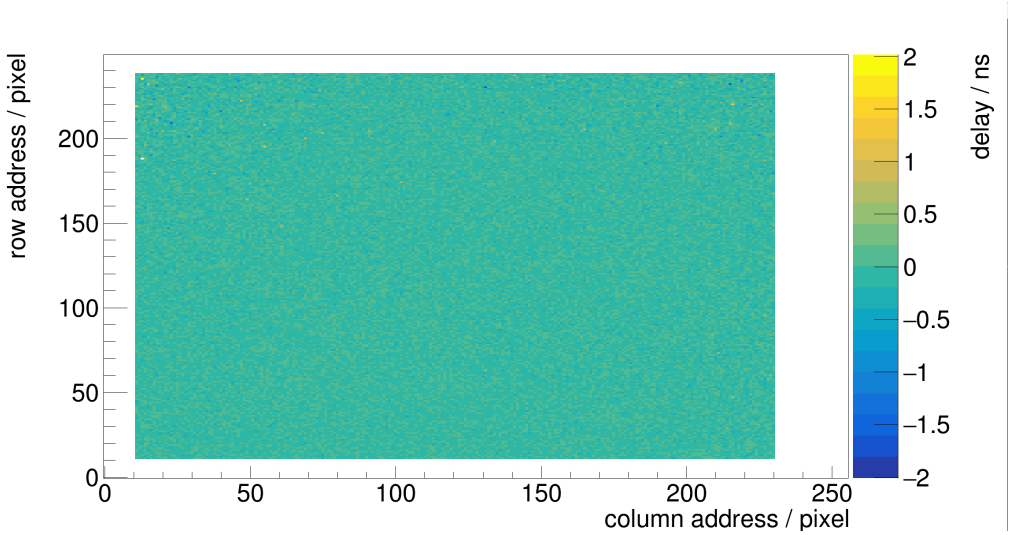

(b) Time-walk and delay corrected

Figure 26: Pixel delay map

Row delay correction

The delay depends on the row of a pixel since for higher rows transmission lines will be longer and have longer shared distances with neighboring transmission lines. Fig. 26a shows that the delay from pixels in the same sector

(Section 7.5) is similar. Therefore, the mean delay of hits in the same row is calculated and fitted linearly for rows of the same sector. Since the rows of each sector are different for odd and even column this is done separately for hits in odd columns and even columns. Each hit is then corrected by its row delay according to these fits.

In terms of performance, the single pixel delay correction is more precise than the row delay correction, as it can correct for each pixel separately. On the other hand, the row delay correction is more practical for an experiment, since it needs less statistics and it is based on a much smaller set of parameters (16 per sensor, against the 64,000 of the single pixel delay correction).

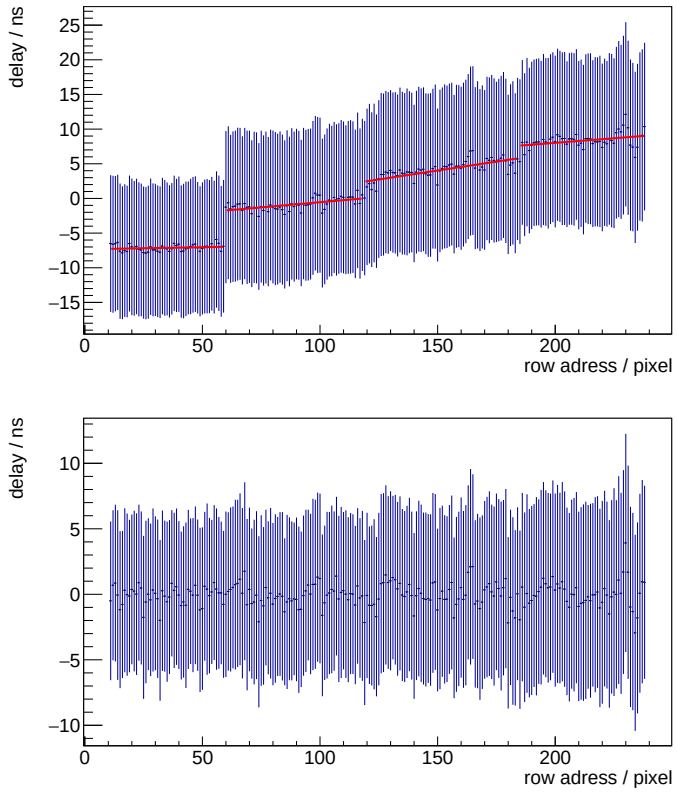

Figure 27: Row delay for odd columns before (top) and after (bottom) time-walk and delay correction.

Unfortunately the delay correction does cancel part of the effect of the time-walk correction and vice versa. This is because the ToT behaviour of each pixel is position dependent. To compensate for this effect an iterative approach is chosen. The following steps are performed eight times:

1. Apply a time-walk correction
2. Then apply a delay correction. This changes the mean latency for every ToT slice.

3. Calculate the remaining delay of each ToT slice and update the time-walk correction parameters by half of this value.

4. Undo both corrections and start again with the updated time-walk correction parameters.

The final correction parameters after the last step are then used for the corrections. Fig. 28 shows that the time resolution is significantly improved by this approach.

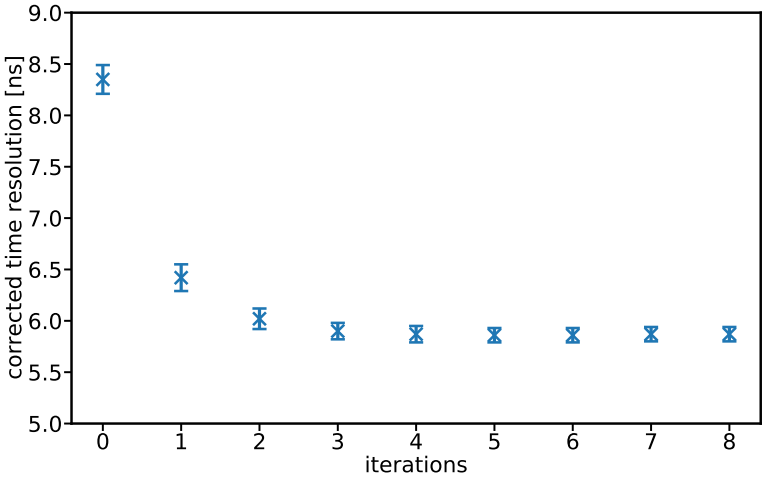

Figure 28: Corrected time resolution versus number of iterations for time-walk and single pixel delay correction

9.3 Abbreviations

In this thesis the name "oscilloscope measurement" will be used with measurements taken with injection hits and oscilloscope, while the measurements taken with the Sr90 method will be divided, depending on the analysis used, into normal analysis (NA) and single pixel analysis (SP).

Part III

Measurement Results

10 Time resolution optimisation studies

10.1 Influence of supply voltages

The MuPix10 is expected to have a similar time resolution as its predecessor, the Mupix8, for which a time resolution of (11.42 ± 0.04) ns uncorrected and

(6.80 ± 0.02) ns corrected was achieved [16]. However, in the first measurements with the MuPix10 a time resolution of (24.7 ± 2.5) ns uncorrected and (13.7 ± 0.5) ns corrected was obtained. The reason for this has been identified in voltage drops in the power distribution of the sensor: a test pad on the insert allows to read out the supply voltages VDDD, VDDA and VSSA at certain positions on the chip. The measurement of these voltages shows that the voltage levels on the chip are much lower than expected. To compensate for this voltage drop the supply voltages are increased to match the values for which the circuits have been designed.

supply voltages measured on	VDDD [mV]	VDDA [mV]	VSSA [mV]
power supply	1800	1800	1200
sensor	1710	1504	919
power supply	1900	2200	1400
sensor	1764	1784	1016

Table 2: Supply voltages measured on power supply and on chip for MuPix10 DACs

Table 3 lists the time resolutions for high and low supply voltages. In addition to the default DAC configuration for MuPix10 also the default configuration for the MuPix8 is tested, since the MuPix8 had a different powering scheme but is similar to the MuPix10 in many other regards. Furthermore, when applying the high supply voltages the ground rises so the baselines BLDig and BlPix and the threshold ThLow have to be increased by the new ground level. For a better comparison the configurations are tested also without adjusting the Threshold and baselines.

DAC values	supply voltages	adjusted Baseline	Timeresolution [ns] uncorrected	corrected
MuPix10 DACs	low	-	24.7 ± 2.5	13.7 ± 0.5
MuPix10 DACs	high	no	21.7 ± 1.9	13.1 ± 0.5
MuPix10 DACs	high	yes	14.6 ± 0.8	9.63 ± 0.26
MuPix8 DACs	low	-	31 ± 5	13.9 ± 0.7
MuPix8 DACs	high	no	25 ± 3	11.5 ± 0.4
MuPix8 DACs	high	yes	15.6 ± 1.0	9.08 ± 0.04

Table 3: Comparison of different DAC and Voltage configurations. High and low supply voltages refer to the voltage levels from Table 2. The DAC settings are listed in Appendix A

For both sets of DAC values the higher supply voltages yield a better time resolution. The MuPix8 DAC settings have a worse uncorrected time resolution than the MuPix10 DAC settings. However, the MuPix8 power settings have the best corrected time resolution. This can be explained by the time-walk which is stronger

for the MuPix8 DAC settings due to VNFB being lower (see Section 11.1.2). Since the MuPix8 DAC values with high supply voltages and increased baseline and threshold levels performs best, it is chosen as the starting point for the further DAC optimisation.

Stripe noise The new configuration introduces noise effects that were not observed with low supply voltages: in the hitmap many hits in consecutive pixels of the same column are visible (Fig. 29). It is not fully understood what causes this kind of noise. Therefore, the influence of different DACs on this kind of noise is investigated. The DAC VNPix which controls the current source for the amplifier has the biggest influence on this kind of noise. It was found that stripe noise does not occur for VNPix=18. However, if one increases VNPix the power consumption of the chip goes up. This leads to higher voltage drops. If one adjusts the supply voltages to compensate for this the stripe noise occurs again. This leads to an upwards spiral of increasing VNPix and adjusting the supply voltages. Therefore, VNPix is increased to 18 without adjusting the supply voltages.

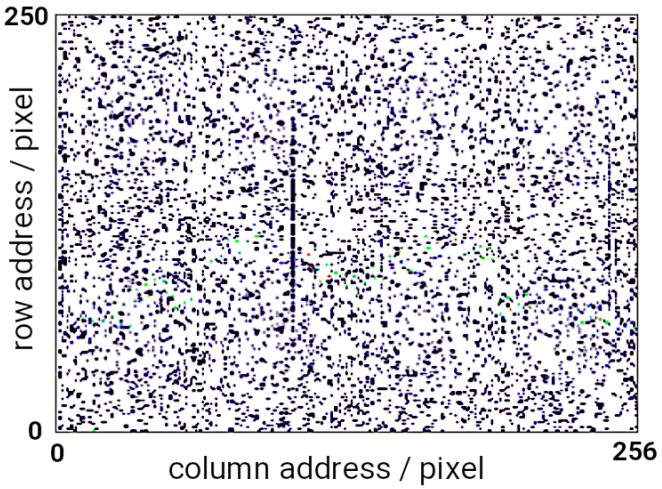

Figure 29: Stripe noise in the hitmap of the sensor

10.2 Threshold dependence of the time resolution

As discussed in the time resolution should improve for lower thresholds. This is also what can be seen in Fig. 30. For an optimal time resolution the threshold has to be chosen as low as possible but still above the noise level. The lowest threshold that could be reached with a sustainable noise rate was 27 mV. Therefore, this threshold is chosen for all further measurements.

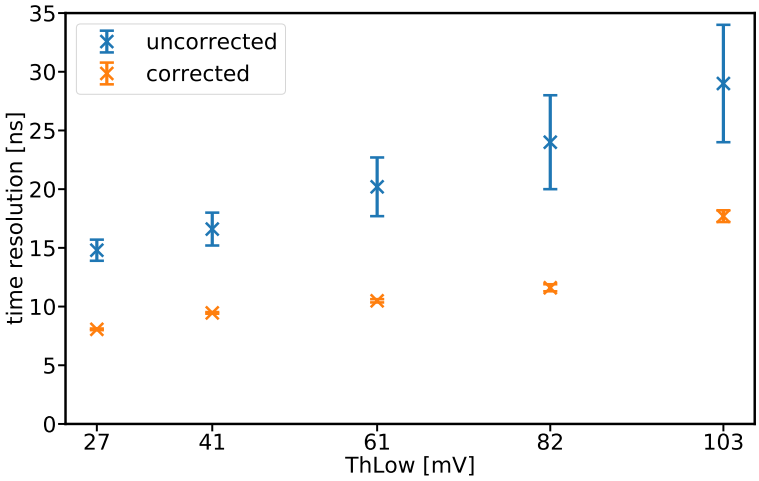

Figure 30: Time resolution for different threshold levels (NA)

10.3 Amplifier DAC optimisation

For the time-walk and the time resolution the signal shaping of the amplifier is critical. Therefore, the influence on the time resolution was measured for the DACs VNFollPix, VNFB and BLResPix, which control the pulse shaping. The DACs are described more thoroughly in Section 7.3.

Figs. 31 to 33 show that the current settings are indeed a good choice and probably only small improvements can be made by fine tuning the DACs. However, since the individual time resolutions are calculated for a fixed injection voltage it is not possible to deduce how the time-walk would effect the time resolution for pulses with a broader ToT spectrum than these generated by a single injection voltage.

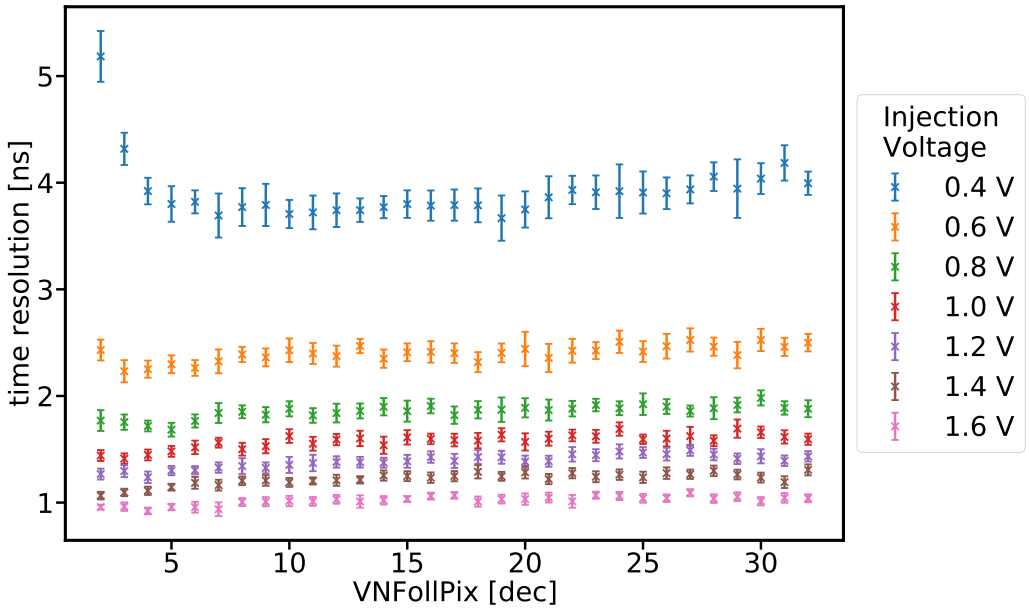

Figure 31: Time resolution measured with oscilloscope for different values of VNFollPix

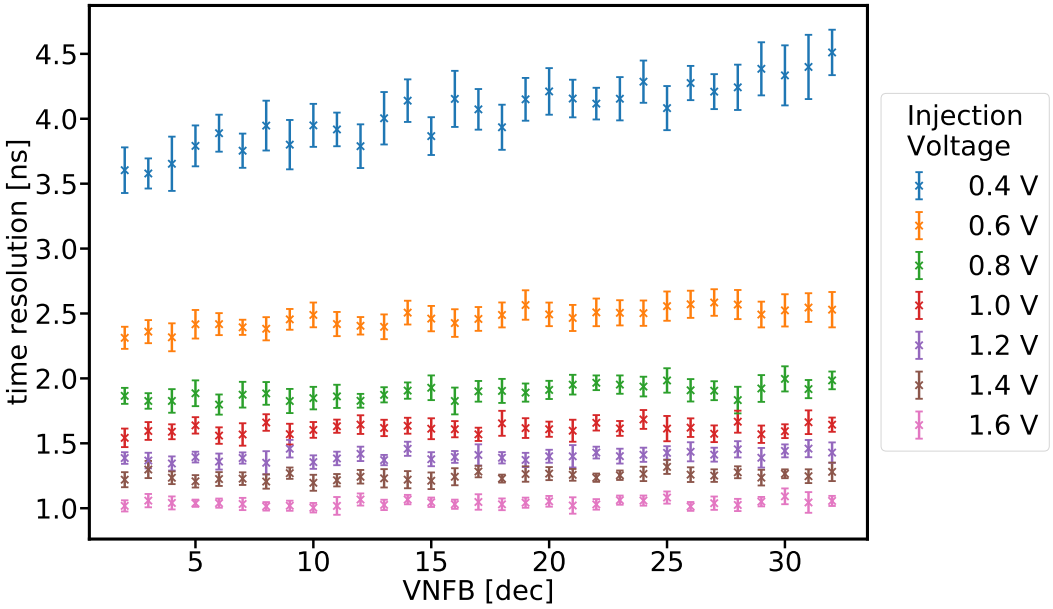

Figure 32: Time resolution measured with oscilloscope for different values of VNFB

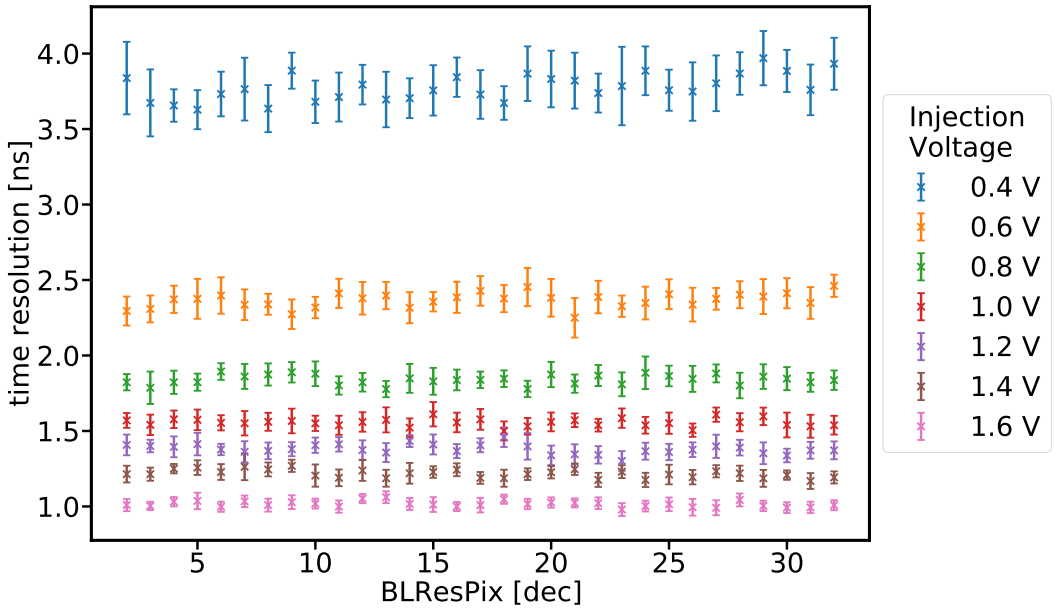

Figure 33: Time resolution measured with oscilloscope for different values of BLResPix

10.4 Resulting configuration

The configuration which results from the optimisations in the previous sections is given in Table 4.

DAC	value [dec]	value [hex]
BLResPix	5	5
VNPix	18	12
VNFBPix	4	4
VNFollPix	12	c
VPLoadPix	10	a
VNOutPix	10	a
VPComp2	5	5
VPTimerDel	1	1
VNTimerDel	20	14
VPVCO	22	16
VNVCO	23	17

Voltage levels	
HV	−100 V
VDDD	1900 mV
VDDA	2200 mV
VSSA	1400 mV
gnda	242 mV
BlPix	1037 mV
BlDig	740 mV
ThLow	767 mV

Table 4: Optimised configuration

11 Characterisation with optimised configuration

This chapter shows the results of the characterisation of MuPix10 performed with the configuration obtained in the previous chapter. The goal of the following characterisation is to find out what features limit the time resolution and identify potential issues which should be fixed in the design of the MuPix11.

11.1 Time over threshold behaviour

The time-walk correction relies on the ToT information. Therefore, the ToT behaviour of the sensor is investigated in this section.

11.1.1 Characterization of the ToT-cap

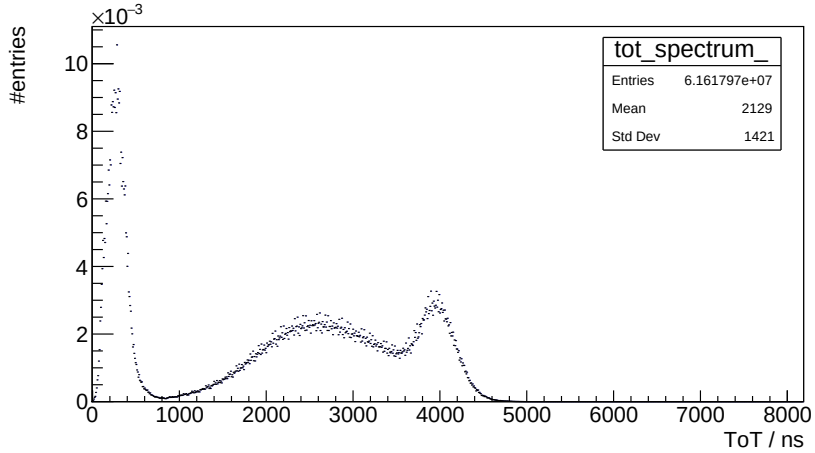

Figure 34: ToT spectrum of Sr90 for VNTimerDel=1 and VPTimerDel=1 (NA)

Fig. 34 shows the ToT spectrum for VNTimerDel=1 and VPTimerDel=1. The peak at the lower end of the ToT spectrum is caused by crosstalk and noise while the peak at the higher end is caused by the ToT-cap (Section 7.4). Measurements of the ToT spectrum of a Sr90 source showed that the ToT-cap decreases as expected for higher values of VNTimerDel and VPTimerDel. The maximum ToT-cap which can be reached is (3950 ± 230) ns for VNTimerDel=1 and VPTimerDel=1. This is not sufficent to observe the whole ToT spectrum. Therefore, for the MuPix11 it is recommended to increase the range of the ToT-cap to allow a better understanding of the time-walk and the ToT behaviour. Also it might be useful if the ToT-cap could optionally be switched off to be sure that the ToT-cap circuitry does not cause strange effects by interacting with other parts of the sensor in an unforeseen way.

An investigation of the ToT-cap performed with the oscillosope (Fig. 35a), shows how the hitbus is temporarily switched off by the ToT-cap as intended. However,

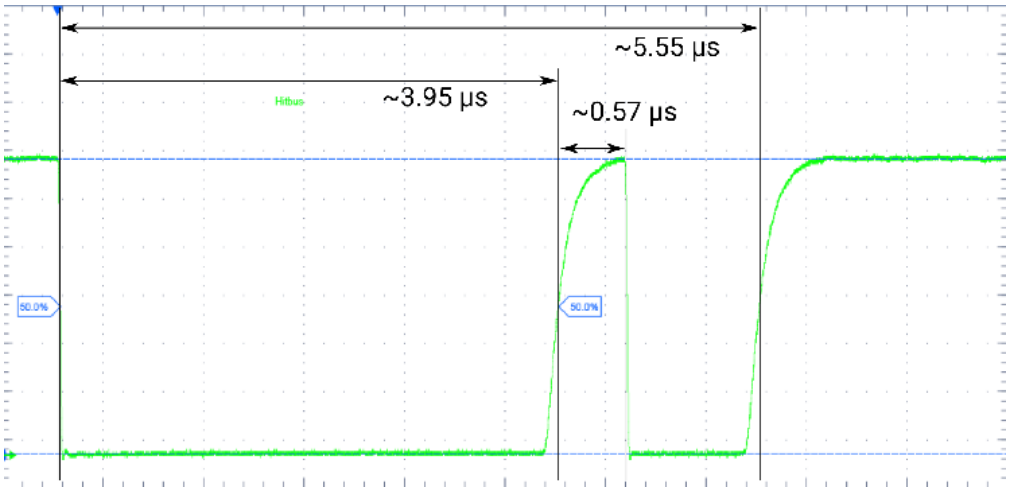

(a) ToT-cap working as intended

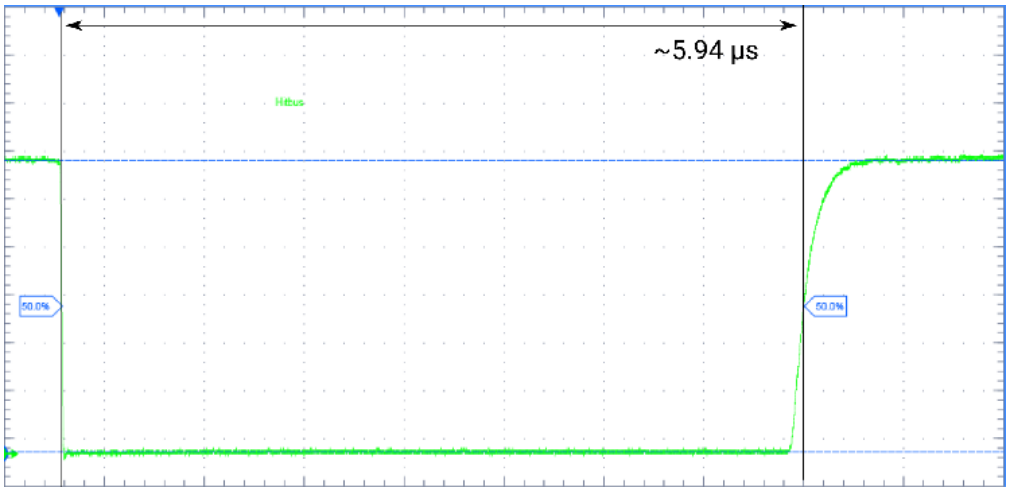

(b) ToT-cap failed to trigger

Figure 35: Hitbus at high injection voltages as observed with the oscilloscope

for large pulses the ToT-cap sometimes does not trigger leading to uninterrupted pulses with ToT higher than the ToT-cap (Fig. 35b).
Further investigations of the the ToT-cap have also shown its column dependency, which was not expected (Fig. 36). The ToT-cap is smaller near the columns 50 and 178. This is near to where the power lines are located. Therefore, it is assumed that power drops over the matrix cause the ToT-cap to increase in pixels farther away from the power lines, because the capacity in ToT-cap circuitry needs longer to charge (Section 7.4).

11.1.2 Influence of the amplifier DACs on the ToT

The ToT-cap for the configuration used in this thesis is about 4 µs. In the final experiment, however, this leads to a long dead time, for which reason different DAC settings with a smaller ToT range might be considered. The two DACs which influence the ToT of the signals are BLResPix and VNFB. In general the

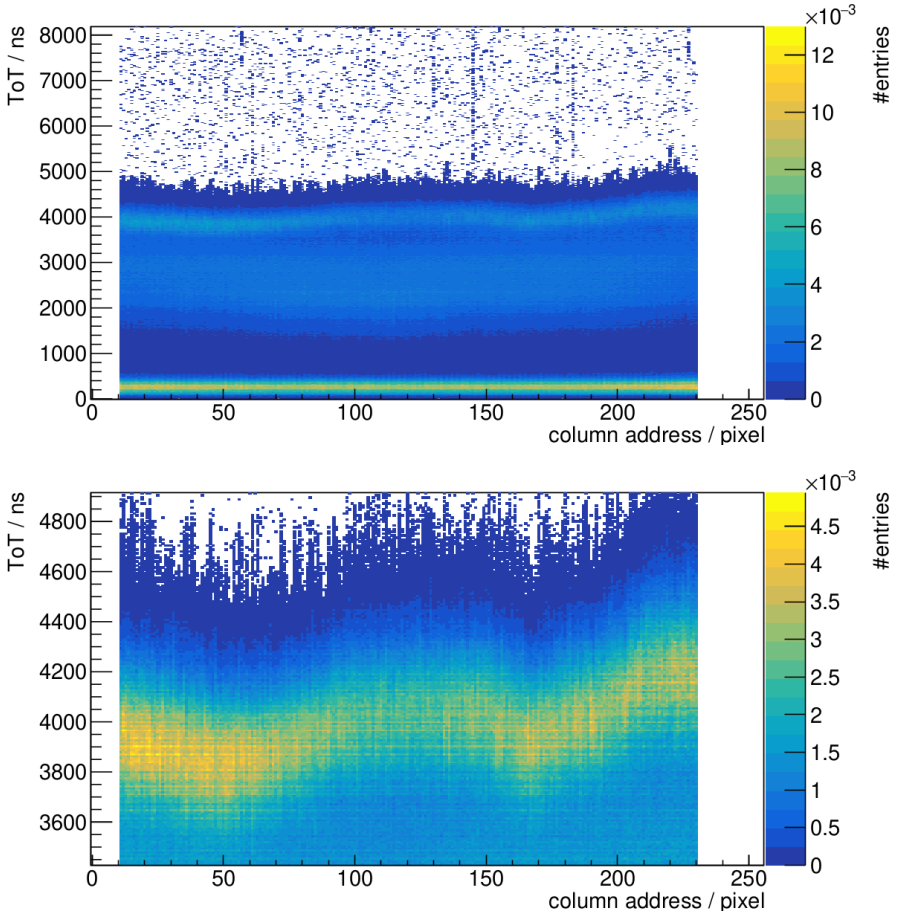

Figure 36: Normalized ToT spectrum for different columns. Top: full spectrum, bottom: zoom over the ToT-cap region

ToT decreases as the value of each DAC increases, as can be seen in Fig. 38. The ToT saturates at the ToT-cap of (3735 ± 15) ns. However, for higher injections the mean ToT increases to values above the ToT cap and also the error increases. This is because the ToT-cap does not always trigger for large pulses (compare Section 11.1.1). The high error reflects the fact that some pulses keep their original ToT while others get interrupted by the ToT-cap as intended.

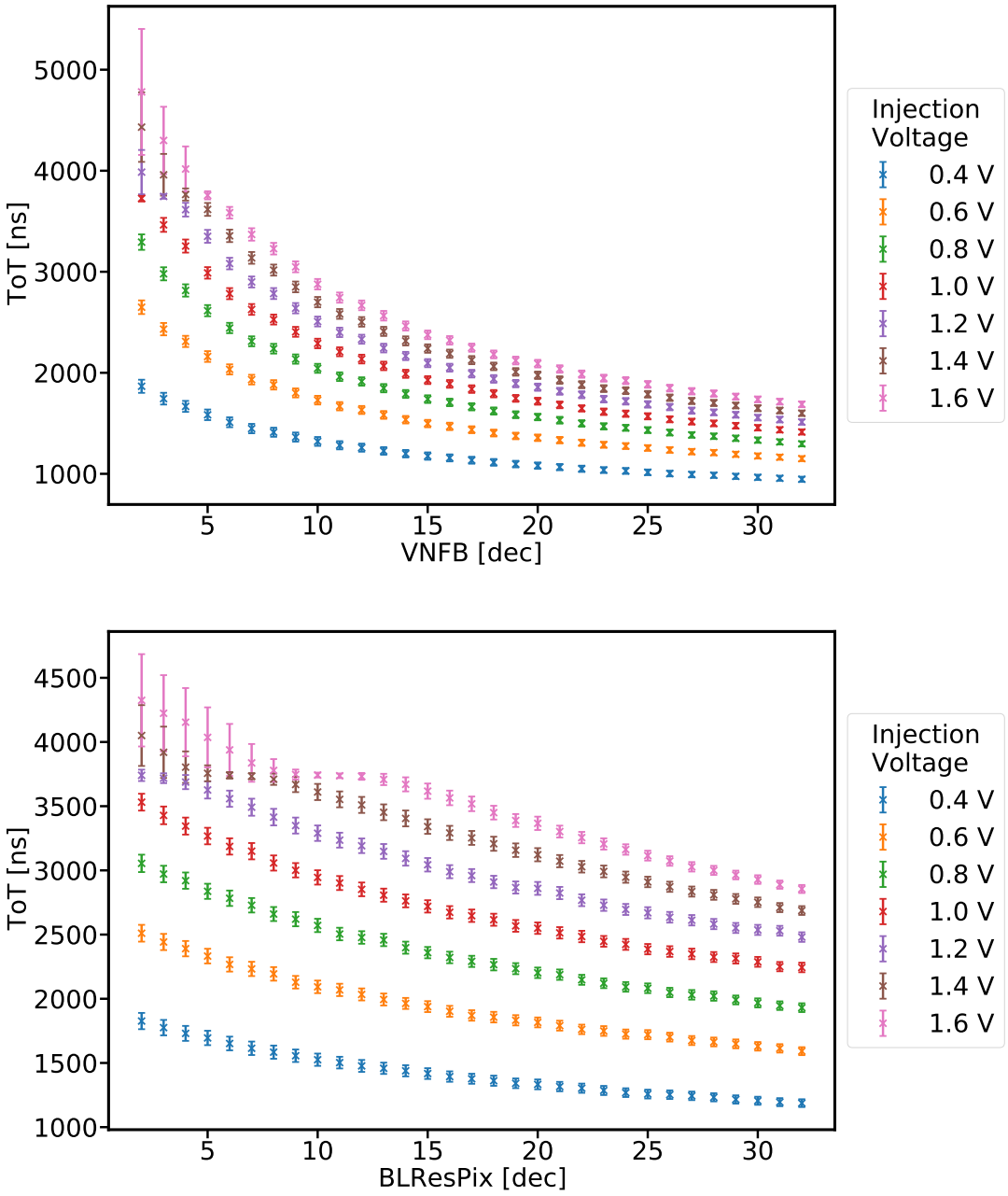

Figure 37: ToT for different dac values measured with the oscilloscope

11.1.3 Spatial dependence of the mean ToT response

When applying a time-walk correction (Section 9.2.1), all pixels are treated together, and therefore the same correction parameters are applied for all of them. It is known, however, that each pixels time-walk behaviour is different due to fabrication variations and the signal shaping in the transmission lines. To investigate this point, the mean ToT for an injection of 0.6 V is measured for pixels in a uniform subset of pixels (Fig. 38a).

The pixels mean ToT response for the same injection varies strongly. Some pixels

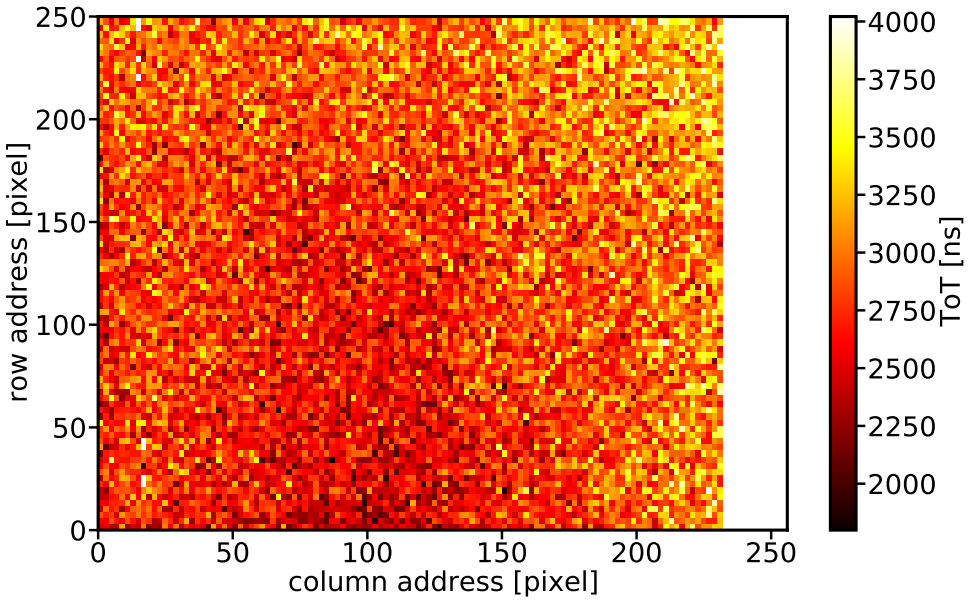

(a) Default configuration

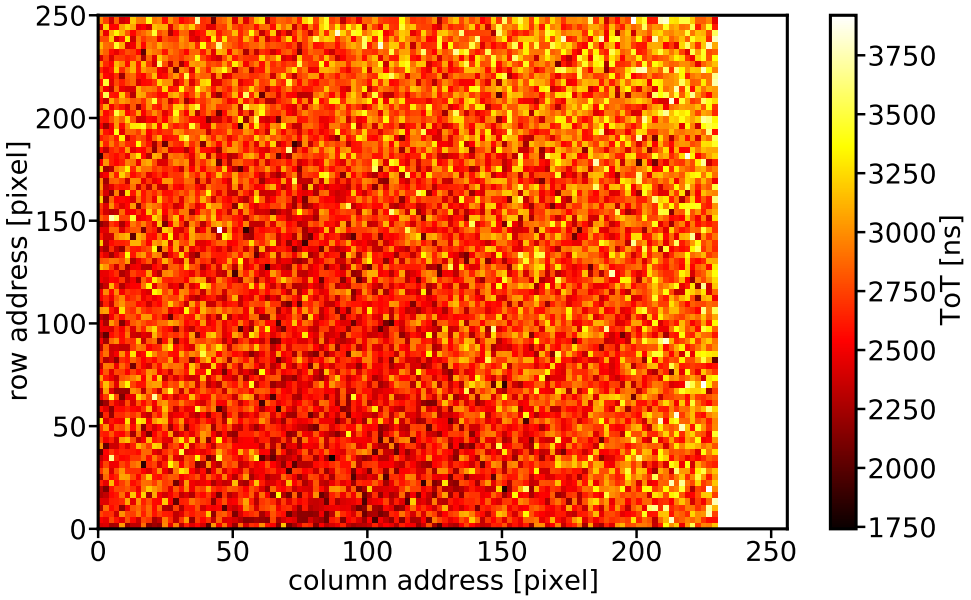

(b) Reduced periphery power consumption

Figure 38: Mean ToT at 0.6 V injection measured with the oscilloscope. Only pixels in even column and every third row were measured, but the spaces between the measured pixels are left out so that the distribution is more clearly visible.

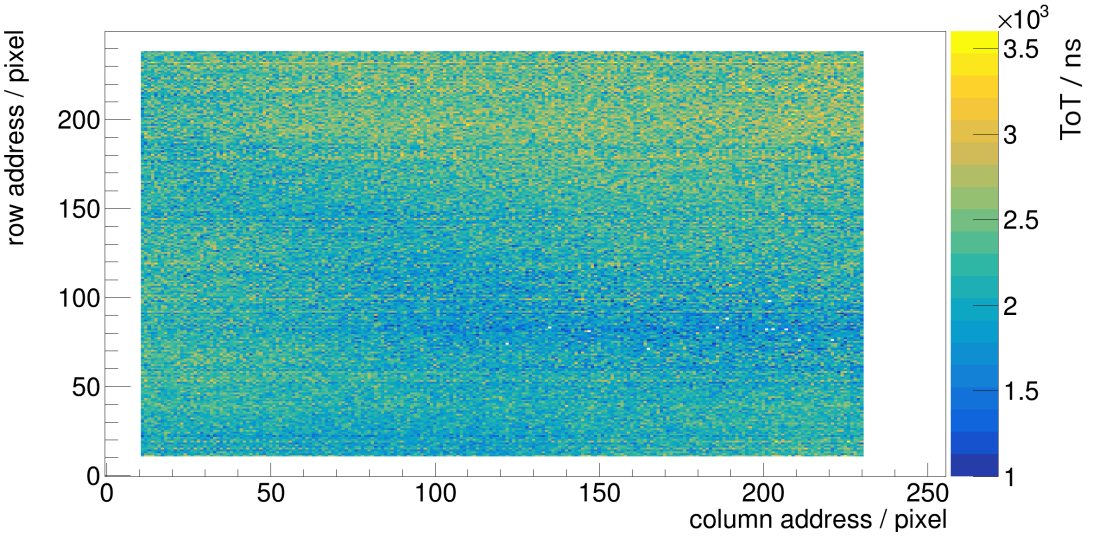

Figure 39: Mean ToT per pixel without crosstalk cut (NA)

are capped by the ToT-cap at about (4020 ± 220) ns while others have a mean ToT of only about (1800 ± 60) ns. The 2-dimensional distribution of the mean ToTs looks similar to the temperature distribution, since the heat is dissipating outwards from the state machine located in the digital periphery. To test this assumption, the measurement is repeated with reduced power consumption in the periphery (Fig. 38b). However, no significant change in the ToT distribution could be observed. The temperature therefore does not affect the distribution. Another possible explanation might again be the power distribution across the pixel matrix. If this is the case it would mean that pixels in higher rows and at the edges have higher ToT because of power drops across the pixel matrix.
The mean ToT of each pixel is also measured with NA (Fig. 39). They are not directly comparable to the ToTs measured with oscilloscope because the oscilloscope uses injection for signal generation instead of an Sr90 source. However, they also show a wide spread in the mean ToT.

11.2 Transmission line delay

To study the row delay behaviour, the mean row delay is obtained with NA (Fig. 40a). In the plot, the four sectors from the routing scheme are clearly visible. The total span of the mean row delay from minimum to maximum is about 16 ns. The routing scheme is designed such that pixels with longer readout lines in the pixel matrix have shorter readout lines in the digital periphery. Therefore, the row delay is almost constant in the lowest sector. In the other sectors the longer lines in the periphery can not compensate the longer lines in the pixel matrix anymore, which explains the linear increase of the row delay in these sectors.

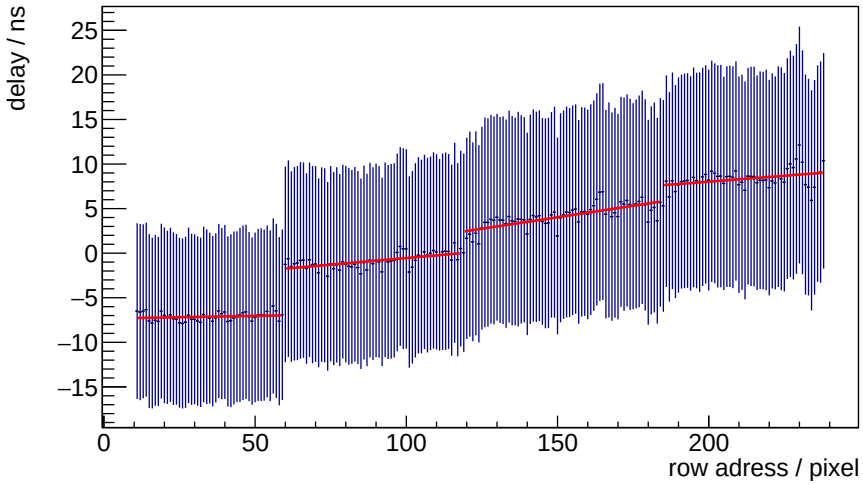

(a) uncorrected

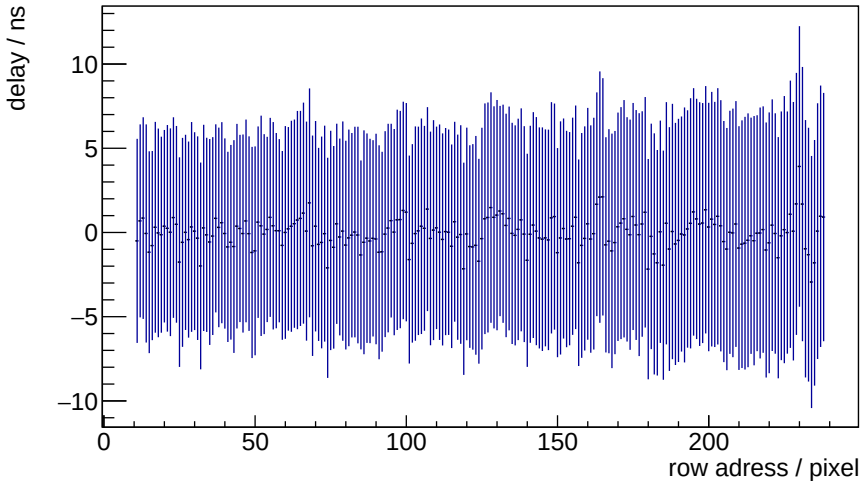

(b) corrected

Figure 40: Row delay for odd columns (NA)

The single pixel analysis yields a delay map which allows to further investigate the pixel delay (Fig. 41). The four sectors and the different ranges for odd and even columns are clearly visible. The span from minimal to maximal delay is almost 80 ns, but the mean delays per row (Fig. 42) agree to a good extent with the results from NA.

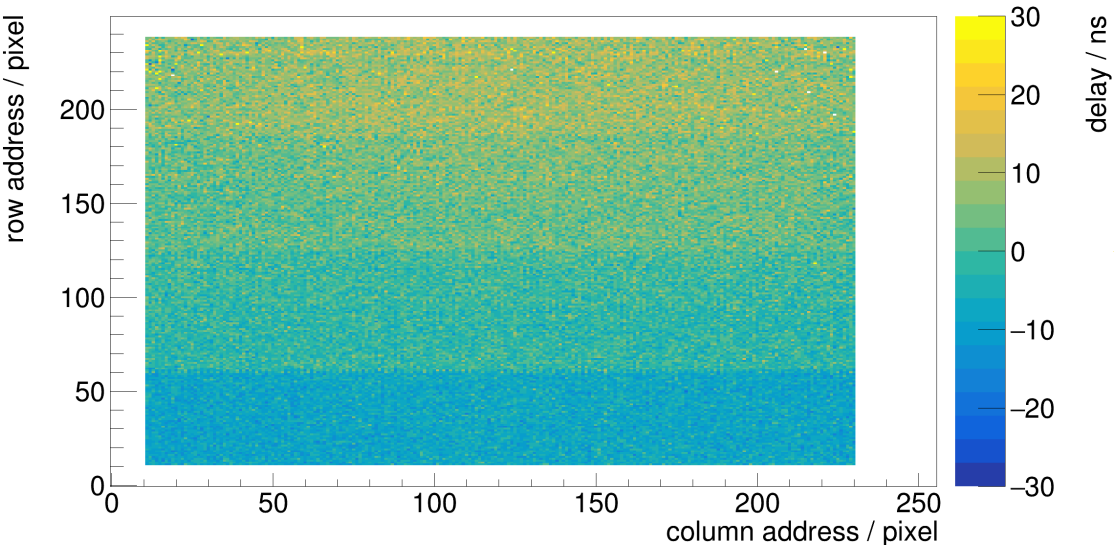

Figure 41: Uncorrected delay map (SP)

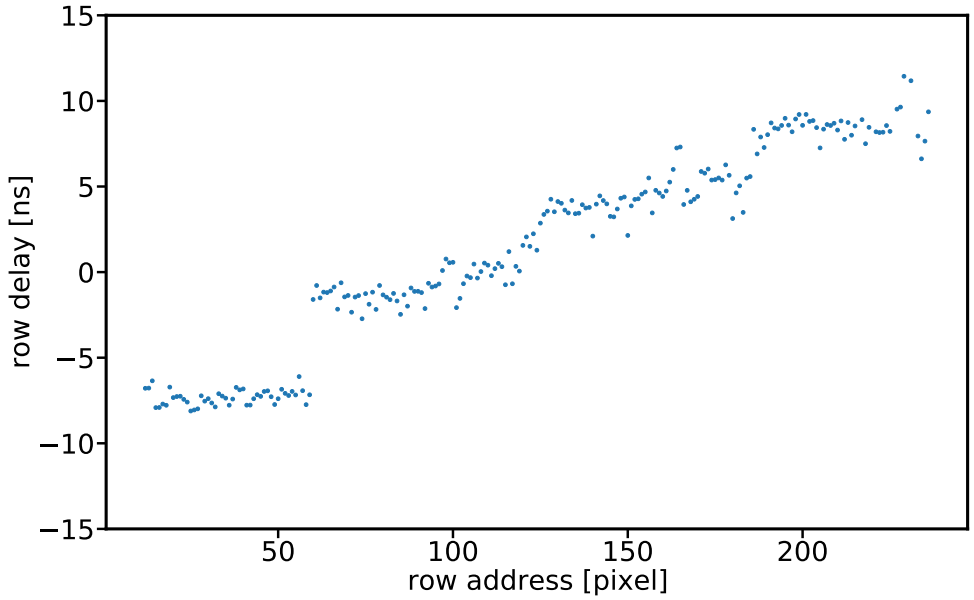

Figure 42: Uncorrected row delay for odd columns calculated from Fig. 41 (SP)

11.2.1 Pixel to pixel delay

To have an estimate of how much the delay of pixels in a certain region is spread out, one can histogram all the delays from that region and fit a Gaussian to the result. The σ of this gaussion is called the pixel to pixel delay (PtP delay). This is performed after time-walk correction to exclude the latency due to time-walk. Fig. 43a shows the PtP delay for different subsections of the sensor. As shown in Fig. 43b, the PtP delay is column-dependent but shows little dependency on the sector (compare Table 5). The mean PtP delay for the full sensor is (5.53 ± 0.06) ns.

Sector	PtP delay [ns]
1	5.75 ± 0.12
2	5.61 ± 0.11
3	5.45 ± 0.08
4	5.46 ± 0.08
Mean	5.53 ± 0.06

Table 5: PtP delay per sector

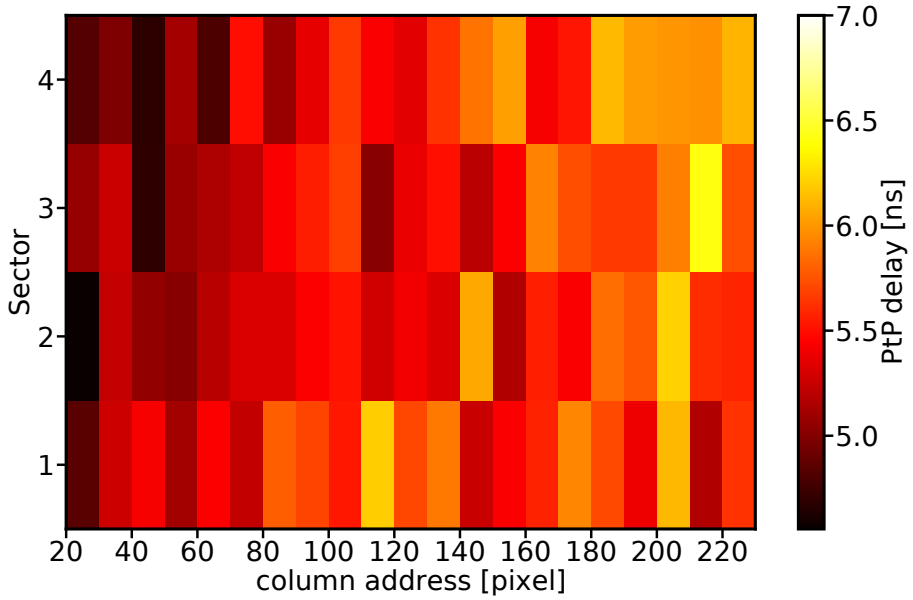

(a) PtP delay in different regions of the sensor

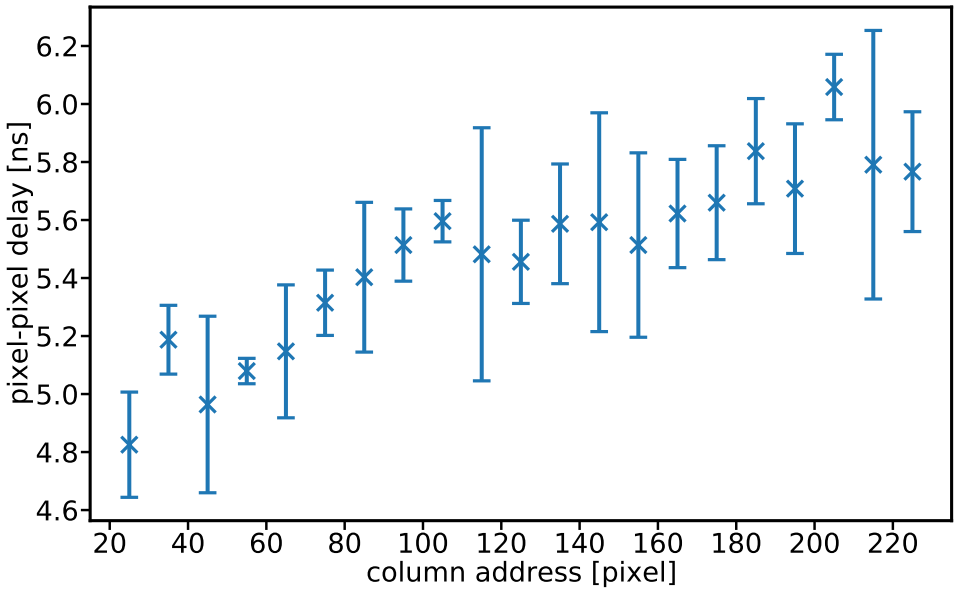

(b) Mean PtP delay per column interval. This is the projection of the plot above.

Figure 43: PtP delay

11.2.2 Injection delay

This section shows the study of the delay performed with oscilloscope and injection. In contradiction to the measurements with NA and SP, there seems to be a delay which increases as the column decreases (Fig. 44a). This indicates that the delay measurements with the oscilloscope may be flawed, since the injection signal measured by the oscilloscope is not taken from the pixel but on the motherboard PCB. Therefore, there seems to be an additional delay caused by the injection signal travelling to the pixel. The shortest injection lines are those in the lower right of the pixel matrix. Therefore, also the delay measured with oscilloscope is smallest there. To compensate for this effect the mean delay of the column is subtracted from each pixel delay (Fig. 44b). Now one can see clearly the four sectors again, but the span of the mean row delay with 40 ns still is much higher than the delay span measured with NA and SP. Therefore, it is suspected that the injection delay is also row dependent. The estimate for the injection delay is about 23 ns from column 0 to 230 and about 24 ns from row 0 to 249.

The previous ToT measurements with oscilloscope are not affected by this, because the ToT is measured using only the hitbus signal. The time resolution measurements are also not affected, since the injection delay is assumed to be constant for each pixel and a constant latency offset does not affect the time resolution.

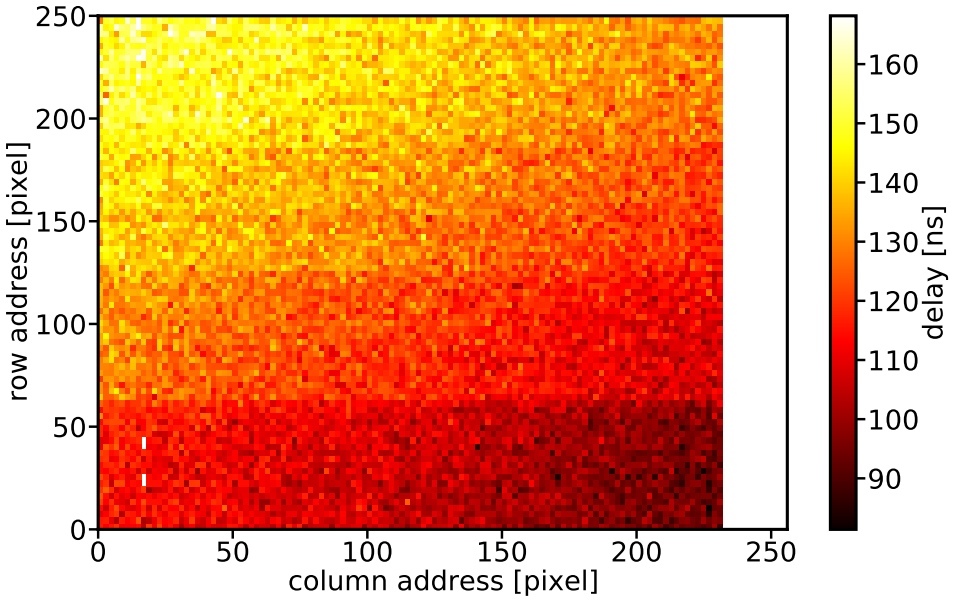

(a) without correction

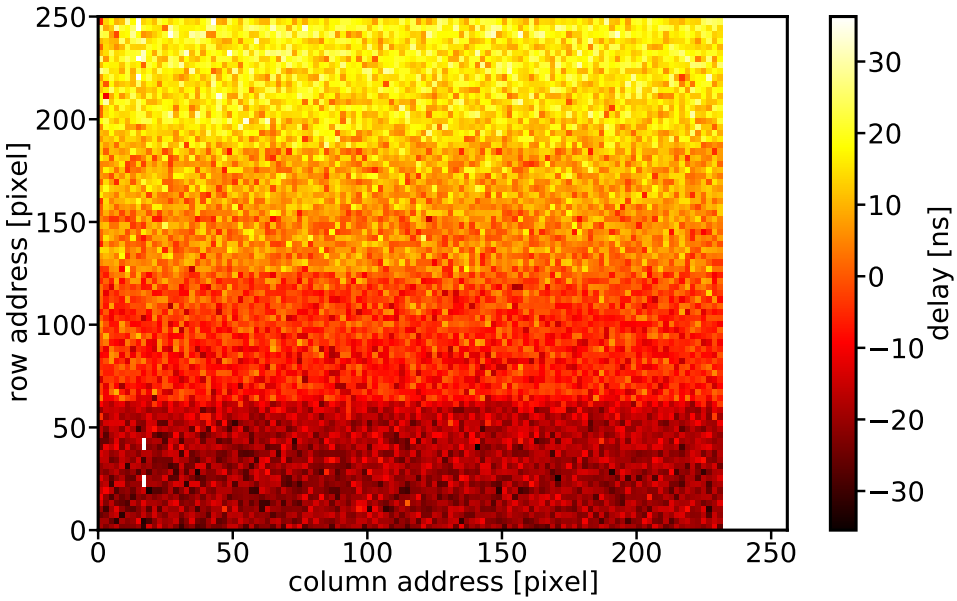

(b) corrected by mean column delay

Figure 44: Hitbus delay measured by oscilloscope. Data is only measured from even columns and every third row but the spaces are filled.

11.3 Time resolution

11.3.1 Single pixel time resolution

Fig. 45 shows the time resolution for each pixel as explained in Section 9.2, the so called single pixel time resolution. The pixels have a mean single pixel time resolution of 6.0 ns with a standard deviation of 1.0 ns as can be seen in Fig. 46. However, the distribution is not symmetric but shows a tail. The time resolution map shows that the pixels with comparatively bad time resolution are located mainly in sector 4 and to a lesser degree in sector 3 (Fig. 45). This is consistent with the mean time resolution in each sector (Table 6) as sector 3 and 4 have significantly worse mean time resolutions than sector 1 and 2. The sector dependence of the time resolutions indicates that signal distortion in the transmission lines causes the higher amount of low time resolution pixels in sectors 3 and 4.

Sector	Mean time resolution [ns]	Standard deviation [ns]
1	5.53	0.7
2	5.41	0.8
3	5.90	1.1
4	6.72	1.5

Table 6: Mean single pixel time resolution per sector. The error of the mean is below 0.02 ns for all sectors.

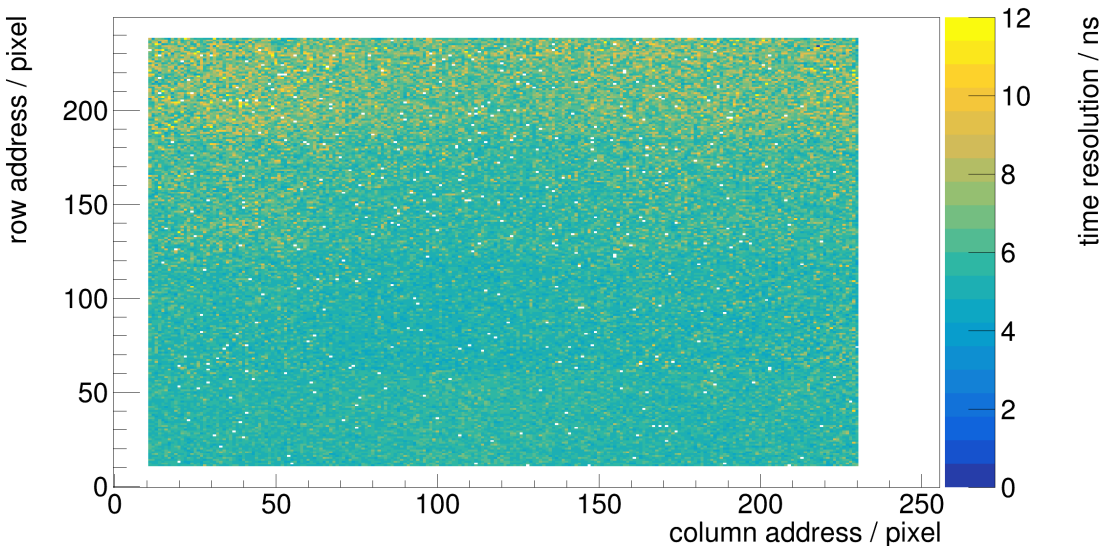

Figure 45: Map of the time resolutions after time-walk and delay correction (SP)

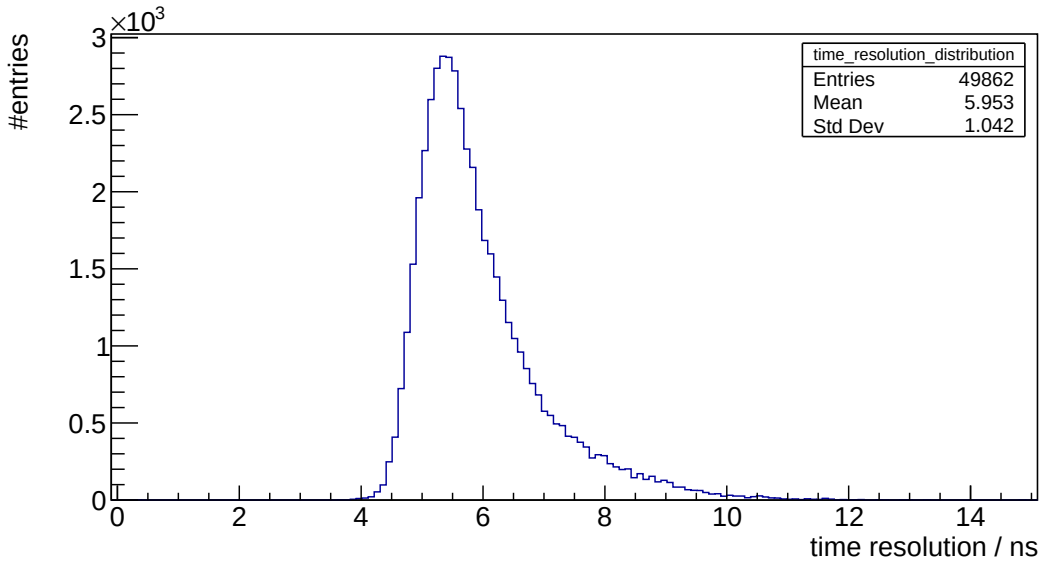

Figure 46: Histogram of the time resolutions of all pixels after time-walk and delay correction (SP)

11.3.2 High voltage dependence of the time resolution

The sensor used for this thesis is 100 µm thick. In the final experiment, however, only thinned sensors with a thickness of 50 µm will be used. It is not clear yet at which high voltages the thinned sensors can be operated. The lower the high voltage the slower is the charge collection and the smaller is the depletion zone, meaning that less charge is collected. This results in a worse time resolution as can be seen in Fig. 47. To get the time resolution of 20 ns required for the Mu3e experiment [2] a high voltage of a least −40 V should be used. However, this value can also be reached with a HV of only −25 V if time-walk and delay correction are applied.

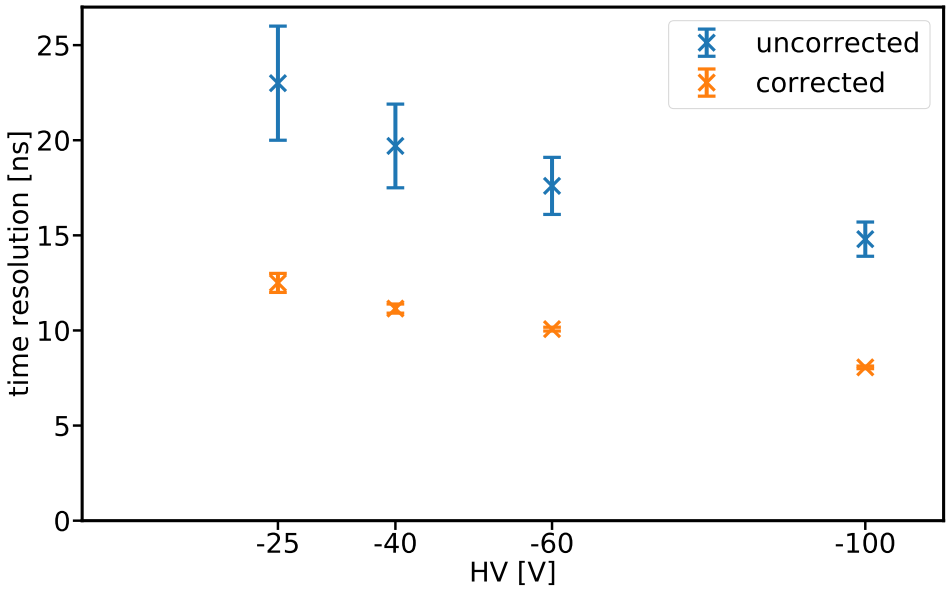

Figure 47: Time resolution for different high voltage levels

11.3.3 Time over threshold depence of the time resolution

The time resolution varies between ToT slices as can be seen in Fig. 48. For lower ToT the rising edge of the signal is less steep. Therefore, noise and small variations of the steepness influence Ts1 much stronger than for higher ToT. Accordingly, the time resolution is better for high ToT than for low ToT. For SP and NA the time resolution gets worse again at ToTs above the ToT-cap of about 4000 ns. This is because hits with much larger ToT than the ToT-cap fall into the same ToT slice as hits with ToT near the ToT-cap. Hence, the time resolution gets worse in these ToT slices due to time-walk between these hits. The oscilloscope measurement is not affected by this as the time resolution is always calculated for hits generated by the same injection voltage.

In Fig. 49 the quadratic differences between the time resolutions measured with the different methods are plotted. NA corrects only the row delay, while SP also corrects the pixel to pixel delay. Therefore, the difference between them is expected to be the PtP delay. The differences are between 4.8 ns and 6.9 ns which agrees with the PtP delay of about 5.5 ns calculated in Section 11.2.1.

Apart from the difference due to different behaviour near the ToT-cap, the main difference between SP and oscilloscope should be the binning contribution of Ts1 which is $\frac{8\,\text{ns}}{\sqrt{12}} \approx 2.3\,\text{ns}$. However, the differences are between 3.8 ns and 11.2 ns. One possible reason for this is that the pulses from the Sr90 source used for SP analysis might be worse than the pulses generated by injection.

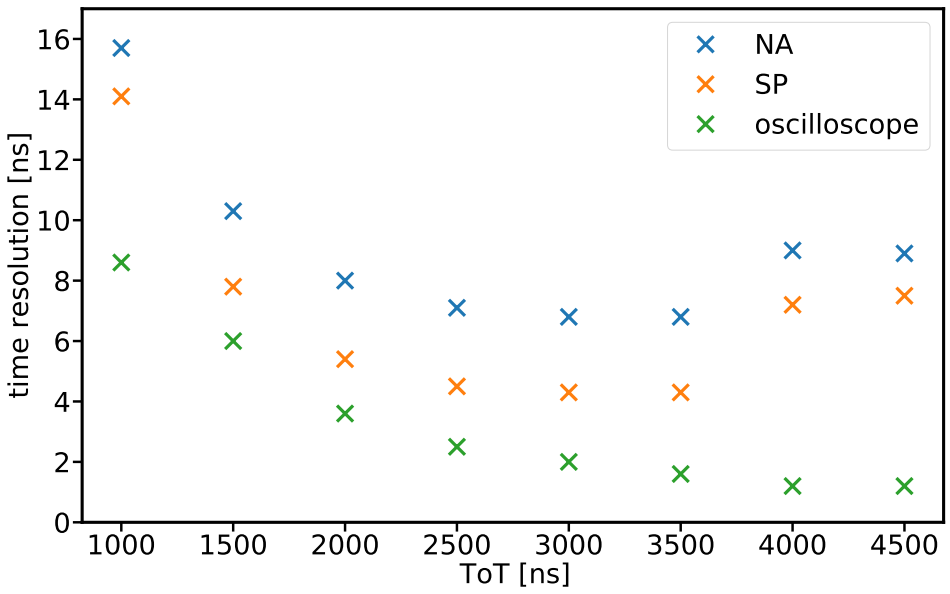

Figure 48: Time resolution for different ToTs

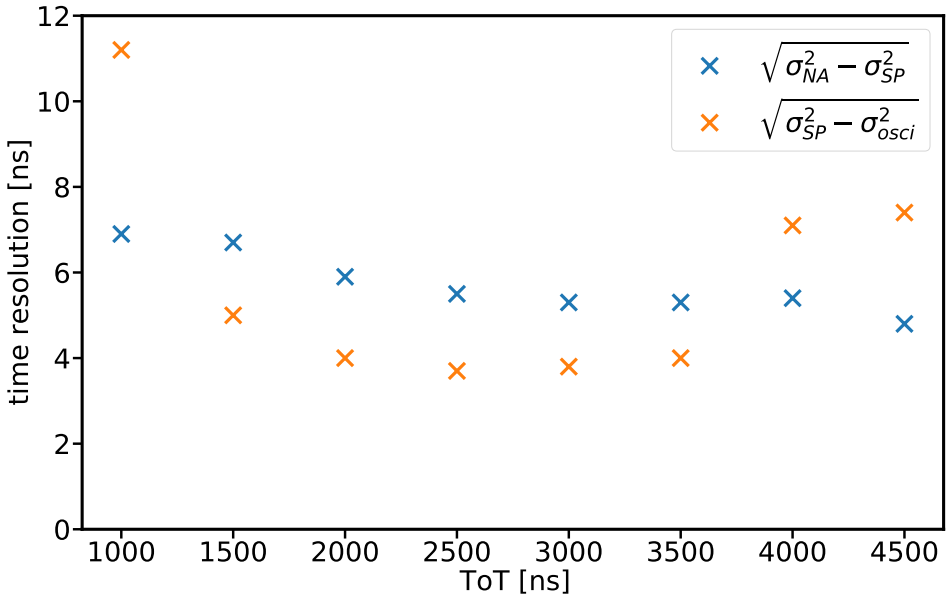

Figure 49: Quadratic differences of the time resolutions for different measurement methods

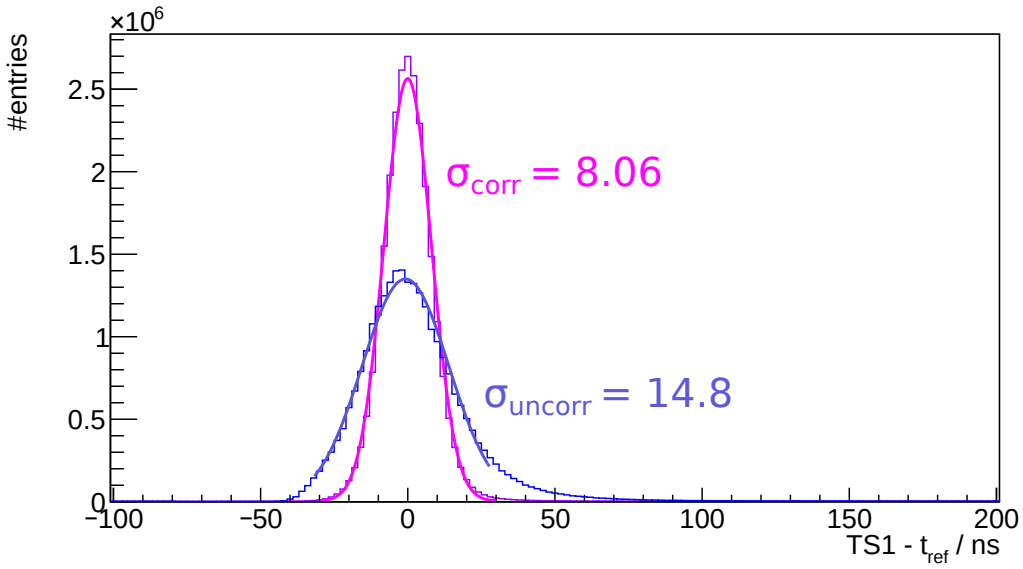

Figure 50: Time resolution before and after corrections (NA)

11.3.4 Full sensor time resolution

The time resolution of the full sensor with the optimised configuration for the Sr90 source is (14.8 ± 0.9) ns uncorrected and (8.06 ± 0.07) ns corrected with NA. With SP analysis even (5.82 ± 0.06) ns can be reached. The quadratic difference between NA and SP is (5.58 ± 0.11) ns, which agrees with the PtP delay measured in Section 11.2.1.

It was found out that with BLResPix=20 a corrected time resolution of (7.02 ± 0.10) ns can be achieved with NA, while the uncorrected time resolution stays the same. This can be explained as follows. At BLResPix=20 the pulses have a smaller ToT than at BLResPix=5 (Section 11.1.2). Therefore, the time resolution at the ToT-cap gets better because less pulses fall into the ToT slices near the ToT-cap and the time-walk range of these pulses is smaller. The investigation of the time resolution with Sr90 as a function of BLResPix is beyond the scope of this thesis. However, for further optimisation of the DAC settings the variation of BLResPix seems to be the most promising approach.

Part IV
Conclusion

12 Summary and conclusion

In this thesis, the MuPix10 configuration is optimised with respect to the time resolution. Furthermore, the sensor is characterised with the goal of identifying the limiting features of the time resolution and finding potential issues which should be fixed in the upcoming MuPix11 which will be the sensor used for the Mu3e experiment.

First, the supply voltages are increased to compensate for internal power drops on chip. With the increased power supply voltages, the default DAC settings used for the previous prototype MuPix8 prove superior in terms of time resolution to the default DAC settings for the MuPix10 defined prior to this thesis at the usual supply voltages. The resulting configuration allows for a threshold level of 27 mV which is the lowest threshold level ever reached on a MuPix sensor. Previous MuPix sensors were operated at threshold levels typically between 50 mV and 100 mV [12, 16]. With the optimised configuration a time resolution of (14.8 ± 0.9) ns uncorrected and (8.06 ± 0.07) ns corrected is achieved. The MuPix8 had a time resolution of (11.42 ± 0.04) ns uncorrected and (6.80 ± 0.02) ns corrected [16].

The time resolution is strongly dependent on the high voltage applied. In order to achieve the time resolution of 20 ns that is required for the Mu3e experiment without corrections, a high voltage of at least -40 V must be applied. With corrections, however, a high voltage of -25 V suffices.

A new feature of the MuPix10, the so called ToT-cap, ensures that all hits are read out within a certain time limit regardless of the ToT of a hit. As a direct consequence, the ToT value is limited as well. However, some issues with the ToT-cap are identified in this work. The ToT range observable with even the highest possible ToT-cap is shorter than the ToT spectrum of a Sr90 source. Therefore, for the design of the MuPix11, the ToT-cap circuitry should allow for larger ToT values, in order to cover the full range of minimal ionising particles. Another issue is that the ToT-cap does not always trigger as intended. Therefore, it might be useful if the MuPix11 allows to switch the ToT-cap off for debugging. Additionally, the ToT-cap shows a column dependency which might be related to power drops over the pixel matrix.

The corrected time resolution is composed of the single pixel time resolution and the pixel-to-pixel delay. The mean single pixel time resolution is 6.0 ns with a standard deviation of 1.0 ns while the pixel-to-pixel delay is (5.53 ± 0.06) ns. They

add up to (8.2 ± 0.7) ns via quadratic addition which is in good agreement with the corrected time resolution of (8.06 ± 0.07) ns.
The single pixel time resolution is sector dependent. The pixels in sector 3 and 4 which are furthest away from the periphery have on average worse time resolutions. This indicates that the distortion of the pulses in the transmission lines plays an important role in the single pixel time resolution.
The pixel-to-pixel delay is observed to be column dependent. The column dependency is similar to the column dependent behaviour of the ToT-cap, which could be explained with power drops over the matrix. Pixels in low columns are in general better powered leading to a lower ToT-cap and less pixel-to-pixel delay. On the one hand, the lower ToT-cap reduces the time resolution, on the other hand less pixel-to-pixel delay improves it. The two effects cancel each other such that the time resolution overall shows no significant column-dependency.
The work of this thesis shows that the MuPix10 satisfies the time resolution requirements for the Mu3e experiment with a proper configuration, which differs from the expected one. The insights into the issues of the MuPix10 gained in this thesis will be beneficial to the design of the MuPix11.

Part V

Appendix

A Configurations

	MuPix10 DACs [hex]	MuPix8 DACs [hex]	Final Configuration DACs [hex]
BLResPix	5	5	5
VNPix	c	f	12
VNFBPix	14	4	4
VNFollPix	a	c	c
VPLoadPix	5	a	a
VNOutPix	f	a	a
VPComp2	d	5	5
VPTimerDel	1	1	1
VNTimerDel	14	14	14
VPVCO	2c	16	16
VNVCO	2d	17	17

Table 7: DAC Configurations used in this thesis

References

[1] G. López Castro G. Hernández-Tomé and P.Roig. "Flavor violating leptonic decays of τ and μ leptons in the Standard Model with massive neutrinos". In: *ArXiv e-prints* (2018), pp. 18, 19. arXiv: 1807.06050.

[2] K. Arndt et al. *Technical design of the phase I Mu3e experiment*. Tech. rep. Mu3e Collabration, Sept. 2020, p. 6. arXiv: 2009.11690.

[3] U. Bellgardt et al. "Search for the decay $\mu^+ \to e^+e^+e^-$". In: *Nucl. Phys.* B299.1 (1988). DOI: 10.1016/0550-3213(88)90462-2.

[4] A. Blondel et al. "Research Proposal for an Experiment to Search for the Decay $\mu \to eee$". In: (2013), pp. 23, 28, 29. arXiv: 1301.6113 [physics.ins-det].

[5] *Standard Model of Elemtary Particles*. WIKIMEDIA COMMONS. URL: https://upload.wikimedia.org/wikipedia/commons/0/00/Standard_Model_of_Elementary_Particles.svg. accessed on the 03/18/2021.

[6] Q. R. Ahmad et al. "Measurement of the Rate of $\nu_e + d \to p + p + e^-$ Interactions Produced by ^8B Solar Neutrinos at the Sudbury Neutrino Observatory". In: *Phys. Rev. Lett.* 87 (7 July 2001). DOI: 10.1103/PhysRevLett.87.071301.

[7] Y. Fukuda et al. "Evidence for Oscillation of Atmospheric Neutrinos". In: *Physical Review Letters* 81.8 (Aug. 1998), pp. 1562–1567. ISSN: 1079-7114. DOI: 10.1103/physrevlett.81.1562. URL: http://dx.doi.org/10.1103/PhysRevLett.81.1562.

[8] F. P. An et al. "Observation of Electron-Antineutrino Disappearance at Daya Bay". In: *Phys. Rev. Lett.* 108 (17 Apr. 2012). DOI: 10.1103/PhysRevLett.108.171803.

[9] M. Menzel. *Calibration of the MuPix10 Pixel Sensor for the Mu3e Experiment*. 2020.

[10] P. A. Zyla et al. "Review of Particle Physics". In: *PTEP* 2020.8 (2020), pp. 34, 537, 541. DOI: 10.1093/ptep/ptaa104.

[11] S. M. Seltzer and M. J. Berger. "Improved Procedure for Calculating the Collision Stopping Power of Elements and Compounds for Electrons and Positrons". In: *International Journal of Applied Radiation and Isotopes* 35 (1984), p. 27. DOI: https://doi.org/10.1016/0020-708X(84)90113-3.

[12] H. Augustin. "Characterization of a novel HV-MAPS Sensor with two Amplification Stages and first examination of thinned MuPix Sensors". MA thesis. Heidelberg University, 2014.

[13] *Pn-junction*. WIKIMEDIA COMMONS. URL: https://commons.wikimedia.org/wiki/File:Pn-junction-equilibrium-graphs.png. accessed on the 03/31/2020.

[14] Ivan Perić. "A novel monolithic pixelated particle detector implemented in high-voltage CMOS technology". In: *Nuclear Instruments and Methods in Physics Research Section A: Accelerators, Spectrometers, Detectors and Associated Equipment* 582.3 (2007). VERTEX 2006, p. 877. ISSN: 0168-9002. DOI: https://doi.org/10.1016/j.nima.2007.07.115. URL: https://www.sciencedirect.com/science/article/pii/S0168900207015914.

[15] *Readout concept of the MuPix sensors*. Mu3e Internal Notes.

[16] J. Hammerich. "Analog Characterization and Time Resolution of a large scale HV-MAPS Prototype". MA thesis. Heidelberg University, 2018.

[17] H. Augustin. "MuPix10: First Results from the Final Design". In: (2020). arXiv: 2012.05868v2 [physics.ins-det].

[18] Tektronix Inc. *DPO7000 Series Digital Phosphor Oscilloscopes Quick Start User Manual*.

[19] A. Weber, H. Augustin, and I. Peric. *MuPix 10 Documentation*. Mu3e Internal Notes. Sept. 2020.

Erklärung

Ich versichere, dass ich diese Arbeit selbstständig verfasst und keine anderen als die angegebenen Quellen und Hilfsmittel benutzt habe.

Heidelberg, den 26. April 2021,